

Evidence for 1.01 s Pulsations of the Central Compact Object in the Supernova Remnant RCW 103 with ASCA, XMM-Newton, and NuSTAR

Kazuo MAKISHIMA^{1,2}, Nagomi Uchida³ and Teruaki Enoto^{4,5}

¹ Department of Physics, The University of Tokyo, 7-3-1 Hongo, Bunkyo-ku, Tokyo 113-0033

² Kavli Institute for the Physics and Mathematics of the Universe (WPI), The University of Tokyo, 5-1-5 Kashiwa-no-ha, Kashiwa, Chiba, 277-8683

³ Institute of Space and Astronautical Science, 3-1-1 Yoshinodai, Chuo-ku, Sagamihara, Kanagawa, 252-5210, Japan

⁴ Department of Physics, Kyoto University, Kitashirakawa Oiwake-cho, Sakyo-ku, Kyoto, 606-8502, Japan

⁵ Extreme Natural Phenomena RIKEN Hakubi Research Team, Cluster for Pioneering Research, RIKEN, 2-1 Hirosawa, Wako, Saitama, 351-0198, Japan

*E-mail: maxima@phys.s.u-tokyo.ac.jp

Abstract

The neutron-star X-ray source 1E 161348–5055, associated with the supernova remnant RCW 103, exhibits clear intensity variations with a period of 6.67 hr. To clarify the nature of this object and its long periodicity, detailed timing studies were applied to its archival X-ray data, taken with ASCA (in 1993), XMM-Newton (in 2001, 2005, and 2016), and NuSTAR (2016 and 2017). It was assumed that the 6.67 hr period arises due to the beat between the rotation and free precession periods of the star that is slightly aspherical. By removing timing perturbations to be caused by this long periodicity, the six data sets consistently yielded evidence for pulsations at periods of $P \approx 1.01$ s, to be interpreted as the objects' spin period, although the optimum energy range differed among the data sets. The measured six periods accurately line up on a linear spin-down trend of $\dot{P} = 1.097 \times 10^{-12} \text{ s s}^{-1}$. The object is implied to have a characteristic age of 14.7 kyr, a spin-down luminosity of $4.2 \times 10^{34} \text{ erg s}^{-1}$ which is insufficient to power the X-ray luminosity, a dipole magnetic field of $\sim 4.6 \times 10^{13} \text{ G}$, and a toroidal field of $\sim 7 \times 10^{15} \text{ G}$. Its similarity and dissimilarity to magnetars are discussed. An emission geometry, which crudely explain these results, is presented.

1 Introduction

The X-ray source 1E 161348–5055, hereafter abbreviated as 1E 1613, is a radio-quiet neutron star (NS) located at the projected center of the supernova remnant (SNR) RCW 103, and once classified as a Central Compact Object (CCO). Although recent studies (De Luca 2017) indicate that it may not be a typical object of this class, we conventionally regard it as a CCO in the present paper. The object was discovered with the Einstein Observatory in 1979 (Tuohy & Garmire 1980), but it then became undetectable. Using the ASCA observatory, Gotthelf et al. (1997), hereafter GPH97, reconfirmed it in 1993 in an X-ray bright state, and in 1997 at a 10% flux level (Gotthelf et al. 1999). On long time scales, 1E 1613 is thus highly variable by up to 2.5 orders of magnitude (e.g., DL06), sometimes emitting long flares (Esposito et al. 2019) and short bursts (Rea et al. 2016). The object thus resembles magnetars (e.g., Rea et al. 2016; Borghese et al. 2018).

The search for a rapid NS rotation in 1E 1613 was performed repeatedly (e.g., GPH97, Gotthelf et al. 1999, De Luca et al. 2007), but none was successful. Instead, with an XMM-Newton observation in 2005, a periodic X-ray intensity variation was found by De Luca et al. (2006), hereafter DL06, at an extremely long period of

$$T = 6.67 \pm 0.03 \text{ hr} = 24.01 \pm 0.11 \text{ ks.} \quad (1)$$

This periodicity had been suggested before (Garmire et al. 2000), and reconfirmed in later observations (Rea et al. 2016; Esposito et al. 2019). Although a straightforward interpretation of this T is

the NS rotation (DL06, Rea et al. 2016), it appears to be way too long, because the implied rotational frequency is $\sim 3 \times 10^{-8}$ of the break-up frequency of a typical NS. It would be difficult to extract the NS's angular momentum to such a nearly zero level. Pizzolato et al. (2008) proposed that 1E 1613 forms a binary with a low-mass companion in a 6.67 hr orbit, and its spin is magnetically locked to the orbital revolution. However, such a binary that survived the supernova explosion is not known.

Before the report of equation (1) by DL06, Heyl & Hernquist (2002), hereafter HH02, tried to explain the earlier suggestion of the long periodicity (Garmire et al. 2000) in the following way. Namely, due to an intense ($\sim 10^{16} \text{ G}$) toroidal magnetic field, this NS is deformed to asphericity of $\epsilon \equiv \Delta I/I \sim 10^{-4}$, where I is the moment of inertia and ΔI is its difference between the parallel and perpendicular directions to the symmetry axis; the NS hence undergoes free precession with a period P , which differs only slightly from the rotation period at $P/(1 + \epsilon)$; the two periods produce a beat effect at a long period of $T = P/\epsilon$ (often called the slip period),¹ which should be identified with equation (1); the pulsation at P must lurk around 1 s; the X-ray emission comes from a displaced hot spot on the NS surface; and some appropriate geometry

¹ “Precession” of an axisymmetric rigid body means the motion of its symmetry axis around the angular momentum vector (Landau & Lifshitz 1996). It occurs with a period close to the rotational period, and their beat appears at 6.67 hr in the present case. Although the beat period itself is sometimes called the precession period, as in HH02, we do not follow this terminology.

can explain the large flux variation at T , while keeping the pulses at P difficult to detect directly. A similar idea was invoked by Zhu & Xu (2006), to explain the suggested ~ 77 min periodicity in the enigmatic bursting radio transient GCRT J1745–3009.

So far, we have accumulated plenty of observational evidence supporting the HH02 scenario. Namely, altogether seven magnetars we studied were all found to exhibit periodical pulse-phase modulation (PPM), in such a way that the arrival times of their hard X-ray pulses at a period P are modulated periodically with a long period T at several tens ks (Makishima et al. 2014, 2016, 2019, 2021ab, 2024ab). Just as HH02 assume, we interpret that these NSs are magnetically deformed to $\epsilon \sim 10^{-4}$, and perform free precession, to produce the PPM at $T \approx P/\epsilon$. This effect is observed exclusively in their spectral hard component, often making their hard X-ray pulsation difficult to detect. Nevertheless, their soft component, being free from the PPM, exhibits a regular pulsation at P . With this knowledge, we can correct (“demodulate”) the photon arrival times of hard X-ray photons for the PPM effect, and securely detect the hard X-ray pulsation.

In the present study, we analyze archival data of 1E 1613, from ASCA, XMM-Newton, and NuSTAR. Guided by our magnetar results, we try to detect the predicted fast ($P \sim 1$ s) pulsation (HH02), by correcting the photon arrival times for the 6.67 hr PPM. In contrast to our magnetar studies where P is known and T is unknown, here T is known and P is unknown,

2 Observations

2.1 Data selection

Although 1E 1613 has been observed by many X-ray satellites, not all the available archival data sets are necessarily suited to the present first-cut attempt, of which the aim is described as above. We hence select data sets that satisfy all the following six criteria; these are considered to provide necessary conditions for a reliable detection of a PPM-affected fast pulsation.

- (i) The observation was made with adequate imaging information, so that we can reduce the background. Those taken with the Suzaku HXD are hence excluded, because the signal intensity from 1E 1613 (even when it was rather bright) will be at most a few percent of the HXD background, which is of the level of ~ 7 mCrab at 15 keV. Although the HXD afforded the detection of periodic pulse-phase modulations from several magnetars, they were considerably brighter than 1E 1613.
- (ii) The data have a modest ($\lesssim 10\%$ at 5 keV) energy resolution, because the PPM in magnetars often show complex energy dependence (Makishima et al. 2024a), which requires us to carefully choose the energy range to be analyzed.
- (iii) The data have a time resolution better than ~ 25 ms, so that the 4th harmonic, which is of vital importance (Makishima et al. 2024a), of the putative $P \sim 1$ s pulsation is fully resolved. Data from the ASCA GIS and NuSTAR, with time resolutions of 61μ s and $< 65 \mu$ s, satisfy this criterion, while some data taken with CCD detectors are excluded depending on the data read-out mode.
- (iv) The total data span is $S \gtrsim 20$ ks, so as to cover a significant ($\gtrsim 75\%$) fraction of $T = 24.0$ ks. Unless this condition is fulfilled, errors in the PPM correction procedure becomes very large, even if T is fixed. The errors would propagate to the uncertainty in P , and make its identification difficult.
- (v) The data provide a sufficient number of signal photons, which is crudely proportional to $Q \equiv f_x \eta_{\text{net}} A_{100}$, a quantity to be called

a data quality measure. Here, f_x is the 0.5–2 keV flux (in 10^{-12} $\text{erg s}^{-1} \text{cm}^{-2}$), η_{net} is the net exposure in ks, and A_{100} is the instrumental effective area at 5 keV² in units of 100 cm^2 . We then require $Q \geq 40$, because this will give $\gtrsim 3000$ signal photons (under an appropriate spectral assumption), which are adequate based on our experience with the seven magnetars.

- (vi) The data are free from major instrumental artifacts, e.g., event pile ups or dead times. This is because the present analysis is more subject to such artifacts than a simple pulsation search.

The application of these criteria to the available archives have left us the six data sets listed in table 1. The first of them, named ASCA93, was taken in 1993 with the Gas Imaging Spectrometer (GIS) onboard ASCA, while the next three (XMM01, XMM05 and XMM16) with the EPIC-pn camera onboard XMM-Newton in 2001, 2005 and 2016, respectively. The remaining two, NuS16 and NuS17, were taken with NuSTAR in 2016 and 2017, respectively. The six data sets span 24 yrs in total.

Of the six data sets, our primary emphasis is put on ASCA93 which led GPH97 to the 1E 1613 rediscovery, because the object was then very bright (though with $Q \sim 50$; see table 1), and the data have a moderate gross exposure which covers about 2.6 cycles of T . In addition, the GIS (Ohashi et al. 1996; Makishima et al. 1996) is suited to this kind of timing studies, thanks to its high time resolution (61μ s), low and stable background, high hard X-ray efficiency, and insignificant dead time or pile-up effects. In fact, a few novel timing results have been derived from the GIS archive (Makishima et al. 2023, 2024b). The object was observed with ASCA again in 1997 (Gotthelf et al. 1999), but it was then fainter by an order of magnitude, with $Q \sim 7$ which does not meet Criterion (v). The 1997 ASCA data are not analyzed here.

Once a candidate period is found in ASCA93, we use the three XMM-Newton data sets to reconfirm it, and constrain the period change rate \dot{P} with progressive accuracies. Among them, XMM01 was taken when 1E 1613 was half as bright as in ASCA93 (table 1), yielding $Q \sim 45$. In XMM05, the object was rather faint, but the exposure was long enough to give $Q \sim 43$. In addition, this data set is worth analyzing, because it led DL06 to arrive at equation (1). The XMM16 data were obtained in 2016 August (Esposito et al. 2019), when 1E 1613 was as bright as in ASCA93. Although another XMM-Newton observation was made in 2018, we do not analyze this data set, because the employed time resolution of 73.4 ms does not satisfy Criterion (iii).

For sky regions near 1E 1613, the NuSTAR archive provides three data sets, taken in 2016, 2017, and 2018. However, the 2018 data are not useable, because the object was just outside the detector field of view. We hence analyze the remaining two, NuS16 and NuS17. As reported by Esposito et al. (2019), the object was very bright in 2016 ($Q \sim 270$), whereas its flux decreased to a quarter in 2017 ($Q \sim 68$). Obviously, the hard X-ray information from NuSTAR is very important, because the PPM in the seven magnetars was seen only in their spectral hard component which appears at $\gtrsim 10$ keV. Nevertheless, the ASCA and XMM-Newton data (both limited to $\lesssim 10$ keV) still remain valuable, because the previous pulse non-detection from 1E 1613 in these soft energies suggests that the PPM disturbance continues way down to < 10 keV. In any case, we may need to carefully adjust, for each data set, the lower energy limit E_L of the analysis.

The source has been observed 24 times with Chandra, from 1999 to 2024. Among them, 20 data sets are short, $S \leq 18$ ks,

² We assume $A_{100} = 0.24, 0.95, 0.70$, and 0.30 for ASCA GIS, XMM-Newton EPIC, NuSTAR FPMA+B, and Chandra ACIS, respectively.

violating Criterion (iv). Most of these data sets also fail to satisfy Criterion (v). Of the remaining four, one (ID 7619) does not meet Criterion (ii) because the focal plan instrument was the HRI. Other two (ID 970 and 501340) were taken with the ACIS but in the TE mode with insufficient time resolution (3.2 s), against Criterion (iii). We are hence left with the only one data set, ID 500209, taken on 2002 March 3 with the ACIS in the CC mode. The source was moderately bright ($f_x \approx 1.1$), but when combined with the limited exposure ($\eta_{\text{net}} \approx 48.6$) and $A_{100} = 0.3$ for Chandra, we derive $Q \sim 16$ which falls short of Criterion (v). In addition, the effects of event pile up, Criterion (vi), is at present unknown. Thus, no Chandra archive can be used in the present study.

2.2 ASCA observation

The ASCA93 observation was intended for X-ray spectroscopy of RCW 103 using the Solid State Spectrometer (SIS). 1E 1613, which was in the same fields of view of SIS and GIS, was rediscovered by GPH97 on this occasion. A serendipitous object, the 69 ms pulsar AXS J161730–505505, was also in the same GIS field of view (Torii et al. 1998, 2000).

Since the SIS data have a poor time resolution in view of Criterion (iii), we use the GIS data, which were processed in the standard way as in GPH97. We extracted events from 1E 1613 and the 69 ms pulsar separately, within 3' of respective image centroids. The arrival times of individual photons were converted to those at the Solar system barycenter, and events from the two detectors, GIS2 and GIS3, were co-added. Due to the limited angular resolution of the GIS, soft X-rays from the SNR heavily contaminate the CCO events, and to a lesser extent the pulsar data. To avoid this effect, we set $E_L \gtrsim 2.5$ keV.

The nominal upper energy bound of the GIS is $E_U = 10$ keV, but we raise it to $E_U = 12$ keV. This is because the 10–12 keV photons are often useful (e.g., Makishima et al. 2023, 2024b), thanks to the high quantum efficiency of the GIS (Ohashi et al. 1996).

Since 1E 1613 emits short bursts (Rea et al. 2016), we produced 3–12 keV light curves from ASCA93, using 10-s bins, and searched them for burst candidates. However, none was found.

2.3 XMM-Newton observations

From the XMM-Newton archive, we analyze the selected three data sets, XMM01, XMM05, and XMM16, excluding the 2018 data for the reason described in subsection 2.1.

The XMM01 data in fact consist of two subsets, one acquired on September 3, and the other on September 3 to 4. The EPIC-MOS data from neither subset are usable, because they were taken in “Full Frame” mode with 2.6 s time resolution, violating Criterion (iii). In the first subset, EPIC-pn was in “Timing” model, with no imaging information. Based on Criterion (i), we discard this data subset. In the second subset, EPIC-pn was in “Small Window” mode with an adequate time resolution of 5.7 ms. Thus, our XMM01 data consist of EPIC-pn events in the second subset. On this occasion, 1E 1613 was about half as bright as in ASCA93.

In the 2005 XMM-Newton observation in which the 6.67 hr flux variation was clearly identified (DL06), 1E 1613 was rather faint, but we still find $Q \sim 43$ thanks to a long exposure. The EPIC data were acquired in the same modes as in the second 2021 subset. We again utilize only the EPIC-pn data.

On 2016 June 22, the CCO suddenly brightened up, emitting a short burst (Rea et al. 2016). About 2 months later, when the source was still in an active state and nearly as bright as in ASCA93, the XMM16 data were obtained in the same mode as

in XMM05. Through this outburst, the 24 ks flux variation profile changed from single-peaked to double-peaked ones (Rea et al. 2016; Esposito et al. 2019). Therefore, when analyzing the EPIC-pn data from XMM16, we must keep in mind that the source behavior could somewhat differ from those on the earlier occasions, possibly with increased timing noise as in some magnetars (Younes et al. 2017; Makishima et al. 2021b).

From each XMM-Newton data set, we produced an X-ray image, and derived 0.2–15 keV keV events with grade $\lesssim 12$, within 15'' of 1E 1613. Then, the barycentric correction was conducted. These steps utilized the SAS v21.0.0 package. Unless otherwise stated, we set $E_U = 10$ keV, above which there are few signal photons. In these data, the event pile-up is estimated to be negligible.

In these observations, the background was relatively calm, so we did not employ so-called SN filter. To remove flaring particle backgrounds, we produced 100-s bin light curves, using 10–15 keV events, and discarded those bins when the count rate (typically 0.002 c s^{-1}) exceeds 0.05 c s^{-1} . This resulted in a photon loss by $\approx 6\%$ in XMM01 and XMM05, and $< 1\%$ for XMM16.

After removing the particle flares, we searched 10-s binned light curves in 2–10 keV for short-burst candidates, in the same way as for ASCA. At about 6.31 ks from the start of XMM01, we found a candidate bin which contains 32 counts (against an average of 7.2 counts/bin), and removed that bin. However, no such candidates were found in XMM05 or XMM16.

2.4 NuSTAR observations

As described in subsection 2.1, we analyze two data sets of 1E 1613; NuS16 and NuS17. The object was very bright in the former, whereas it became 4 times fainter in the latter (Esposito et al. 2019). The NuS16 data were acquired only 4 days after the activity onset, and 54 days before XMM16. Therefore, the behavior of 1E 1613 in NuS16 may be more strongly subject to the issues pointed out for XMM16.

For each data set, we co-added the events from the two Focal-Plane Modules, and processed them (including the barycentric correction) using HEASOFT version 6.35.1 and CALB 2025.4.15. We excluded about 13% of the NuS16 exposure where the attitude solution suffers large errors. On-source photons were accumulated within 1' of the source position on the X-ray image. The derived number of photons, below and above 10.0 keV, are given in table 1. We searched a 10-s bin light curve in 3–70 keV for short bursts, but none was found in either data set.

3 Data analysis and results

3.1 Basic strategy

3.1.1 Period search range

Our central objective is to search the six data sets for a fast ($P \sim 1$ s) X-ray pulsation, assuming that it is not directly visible, due to the PPM disturbance with the period of $T = 6.67 \text{ hr} = 24.0 \text{ ks}$. We try to remove the suspected PPM effects by two methods (subsection 3.3). One is newly developed for the present study, while the other, called “demodulation analysis”, has been applied extensively to our magnetar studies (section 1).

In Makishima et al. (2024a), the P/T ratios of the seven magnetars distribute over $(0.58 - 5.0) \times 10^{-4}$. Then, if the present CCO with $T = 24.0 \text{ ks}$ is in a similar condition, its pulsation is expected to lurk in a range from $P \sim 1.4 \text{ s}$ to $\sim 12 \text{ s}$. Allowing for sufficient margins, we start our period search, with ASCA93, over the range from 0.3 s to 30 s. This interval is made narrower later on.

Table 1. Archival data sets utilized in the present study.

Data set	Instrument	Obs ID	Observation Date (y/m/d)	MJD	Exposure (ks)*		Number of photons†	Flux‡	$Q^{\#}$
					Gross	Net			
ASCA93	ASCA GIS2+3	50035000	1993/08/17	49216	63.4	39.5	79954	5249	5.2
XMM01	XMM-Newton pn	0113050601	2001/09/03	52155	19.6	18.5	17246	7446	2.6
XMM05	XMM-Newton pn	0302390101	2005/08/23	53605	87.9	82.6	21556	5752	0.6
XMM16	XMM-Newton pn	0743750201	2016/08/19	57619	81.0	81.0	159706	75940	4.8
NuS16	NuSTAR FPMA+B	90201028002	2016/06/25	57565	129.6	65.9	37910	2808	5.9
NuS17	NuSTAR FPMA+B	30301017002	2017/06/02	57906	130.5	65.6	9588	1131	1.6
									68

* The gross exposure means the total data span. The net exposure for XMM-Newton is after removing background flares.

† Background-inclusive counts from the CCO. For ASCA and XMM-Newton, “Soft” and “Hard” mean 1–2.5 keV and 2.5–10 keV, respectively. Those of NuSTAR refer to 3–10 keV and 10–60 keV. The “Soft” counts of ASCA93 include the SNR contamination.

‡ 0.5–2 keV flux of 1E 1613, in 10^{-12} erg s $^{-1}$ cm $^{-2}$, from DL06 and Esposito et al. (2019).

The data quality measure, defined in subsection 2.1.

3.1.2 Periodograms (PGs) and Z_m^2 statistics

Our analysis tool is periodogram (hereafter PG), which displays periodicity significance against the trial period P with which the data are epoch-folded. The periodicity significance is expressed by the Z_m^2 statistics (Brazier 1994); at each P , the Fourier power of the folded profile is summed from the fundamental to the m -th harmonic, and normalized by the total photon number, to yield a quantity called Z_m^2 . This is similar to, but improves over, the more conventional chi-square evaluation (Makishima et al. 2023). Based on our magnetar studies, we mostly use $m = 4$, but sometimes $m = 2$ or $m = 3$. For white noise data, Z_m^2 follows a chi-square distribution with $2m$ degrees of freedom (d.o.f); its standard deviation is $\sqrt{4m}$ around the mean of $2m$.

To calculate a PG, usually the observing window function is folded together with the photon counts, and the former is used for exposure correction. However, the periods of interest in the present study are short enough for the exposure to be uniform to within a few percent across the pulse phase (Makishima et al. 2021b). Therefore, the exposure correction is not performed. The original photon counts are hence preserved, and the statistical fluctuations are solely Poissonian.

3.1.3 Period increment steps

In calculating a PG, we scan the period P with an incremental step ΔP which is given as

$$\Delta P = \frac{P^2}{\eta S} \iff \frac{S}{P} - \frac{S}{P + \eta(\Delta P)} \approx 1, \quad (2)$$

considering Fourier independence of adjacent periods. Here, S is the data span (gross exposure in table 1), and η is an “over sampling factor”; $\eta = 1$ means the exact Fourier wavenumber relation, and $\eta > 1$ an over sampling. When the period range is not too vast, the epoch-folding analysis provides a better sensitivity than the Fourier transform scheme, because of the freedom to select $\eta > 1$, and of the capability to incorporate the higher harmonics by selecting $m > 1$.

3.1.4 Period change rate

Since \dot{P} of the putative pulsation is at first unknown, the analysis of ASCA93 and XMM01 are first carried out assuming $\dot{P} = 0$. After an estimate of \dot{P} is found, we iterate these analyses considering \dot{P} , to derive the final results to be presented here. However, the results are nearly the same as the first-round outcomes.

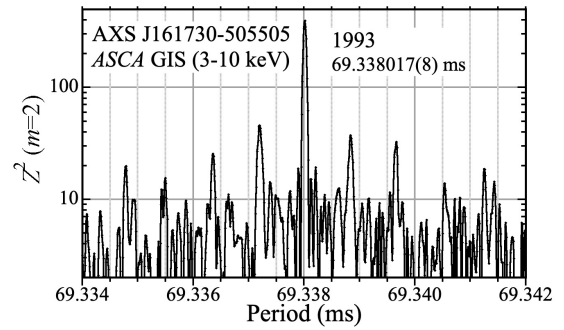


Fig. 1. A PG ($m = 2$) of the 69 ms pulsar AXS J161730–505505, from the 3–10 keV ASCA93 data. The ordinate is logarithmic, to show side lobes. Alt Text: A periodogram of the 69 millisecond pulsar from ASCA93.

3.2 The 69 ms pulsar

Prior to the study of 1E 1613, we analyzed the ASCA93 data of the 69 ms pulsar, AXS J161730–505505, with a few objectives in mind. One is to validate our timing analysis framework using this object that has a known periodicity, and another is to prepare a counter example that is considered to be free from the PPM disturbance. For these purposes, this pulsar indeed provides ideal reference data, which are subject to the same systematic effects (e.g., data gaps and background variations) as the CCO data.

The derived PG is shown in figure 1. After Torii et al. (1998), we employed $\dot{P} = 1.31 \times 10^{-13}$ s s $^{-1}$ and the 3–10 keV energy band; the latter is to avoid the SNR contamination which is still present at the position of this object. We also chose $m = 2$ based on the reported simple pulse profile. The 69 ms pulsation is clearly seen, and the measured period given in the figure is fully consistent with those in Torii et al. (1998). A series of side lobes seen on both sides of the peak are due to the orbital period (5.6 ks) of ASCA.

The analysis of the pulsar data indicated that $\eta \approx 5$ is optimum in equation (2), to reconcile the calculation time with the requirement not to miss any PG peaks. This constitute the third objective of analyzing the pulsar data. We hence employ $\eta \sim 5$ to $\eta \sim 10$ for the study of 1E 1613.

3.3 1E 1613 in the 1993 ASCA data (ASCA93)

3.3.1 Raw periodograms

Using the CCO photons in ASCA93, we calculated a PG over 0.3 s to 30 s (subsubsection 3.1.1), again in 3–10 keV and with $m = 2$ as a first attempt. The derived “raw” PG exhibited many peaks with similar heights up to 35.3, but none were dominant. Thus, in ASCA93, we find no evidence for regular pulsations of 1E 1613 in

the relevant period interval. This is consistent with various previous works (e.g., GPH97), in which no fast periodicity was found even though the attempts were often more thorough than ours.

3.3.2 Periodograms considering pulse-phase modulation

Even if a putative fast pulsation is phase-disturbed by the PPM, the pulse-phase alignment will be recovered if we use those photons which fall in a limited phase of the cycle in T . (This is similar to the case of a pulsar in a binary.) We hence divide all CCO photons in ASCA93 into M_{seg} (a positive integer) subsets. The i -th subset ($1 \leq i \leq M_{\text{seg}}$) comprises those photons of which the arrival time t satisfies $(i-1)/M_{\text{seg}} \leq [t/T] < i/M_{\text{seg}}$, where $[t/T]$ means t modulo T . Then, we calculate PGs, one from each subset, and sum up the M_{seg} PGs into a single PG. If M_{seg} is too small, the PPM effect would still remain, whereas the sensitivity to a hidden periodicity would decrease if M_{seg} is too large. This method is hereafter called “phase-sorted PG”. As a drawback, any intrinsic peak in the PG will be accompanied by many side lobes, because each data subset suffers artificial data gaps repeating every T .

We applied this new analysis to the ASCA93 CCO data, changing M_{seg} from 3 to 10, and E_{L} from 3.0 keV down to 2.0 keV. Also, $E_{\text{U}} = 10$ keV and $E_{\text{U}} = 12$ keV were tested. These PGs consistently revealed a pair of peaks, which became most prominent for $M_{\text{seg}} = 5$, $E_{\text{L}} = 2.5$ keV, and $E_{\text{U}} = 12$ keV. The result under this condition is presented in figure 2a, where the ordinate represents ΣZ_4^2 , i.e., the Z_4^2 values summed over the constituent five PGs. The plot excludes the $10 < P \leq 30$ s period range, where no interesting feature was seen.

Figure 2a clearly reveals the aforementioned pair of peaks, denoted as A and B, of which the parameters are given as

$$A : \Sigma Z_4^2 = 115.5, P = 0.5046777(4) \text{ s} \quad (3a)$$

$$B : \Sigma Z_4^2 = 111.2, P = 1.0093558(8) \text{ s} \equiv P_{93}. \quad (3b)$$

The two periods are in the 1:2 harmonic ratio well within the errors. Thus, B can be regarded as the fundamental of an intrinsic periodicity in the data, and A its second harmonic (half in period and twice in frequency). However, the heights of the two peaks with $m = 4$ are not independent, because they are both contributed by the Fourier components with periods $P_{93}/2$ and $P_{93}/4$.

Figure 2c expands the PG in panel (a) around P_{93} of equation (3b). For easy comparison of the results with different M_{seg} , the ordinate was converted to a new variable Y defined as

$$Y \equiv \frac{\Sigma Z_4^2 - 8M_{\text{seg}}}{4\sqrt{M_{\text{seg}}}}. \quad (4)$$

Since Z_4^2 has the mean as $2m = 8$ and the standard deviation as $\sqrt{4m} = 4$, we expect ΣZ_4^2 , which sums M_{seg} independent variables, to have a mean of $8M_{\text{seg}}$ and a standard deviation of $4\sqrt{M_{\text{seg}}}$. Hence, this equation expresses a procedure of subtracting the mean and normalizing to the standard deviation. As a result, Y represents the conventional “sigma” value.

In figure 2c, PGs with different M_{seg} commonly show a peak at P_{93} . Even the $M_{\text{seg}} = 1$ result, identical to the raw PG, reveals a peak reaching $Y = 6.77$ (or $Z_4^2 = 35.1$), which is not much lower than that ($Y = 8.09$) for $M_{\text{seg}} = 5$. Although this is in an apparent contradiction to the pulse absence in § 3.3.1, this paradox has a clear solution. As M_{seg} increases, the distribution of ΣZ_4^2 starts deviating from chi-square functions, and approaches a Gaussian due to the central limiting theorem. Depending on M_{seg} , the same value of Y translates to very different probabilities; for example, $Y = 7$ means an upper probability of 1.76×10^{-5} if $M_{\text{seg}} = 1$ ($Z_4^2 = 36.0$), but it decreases with M_{seg} , finally converging to the

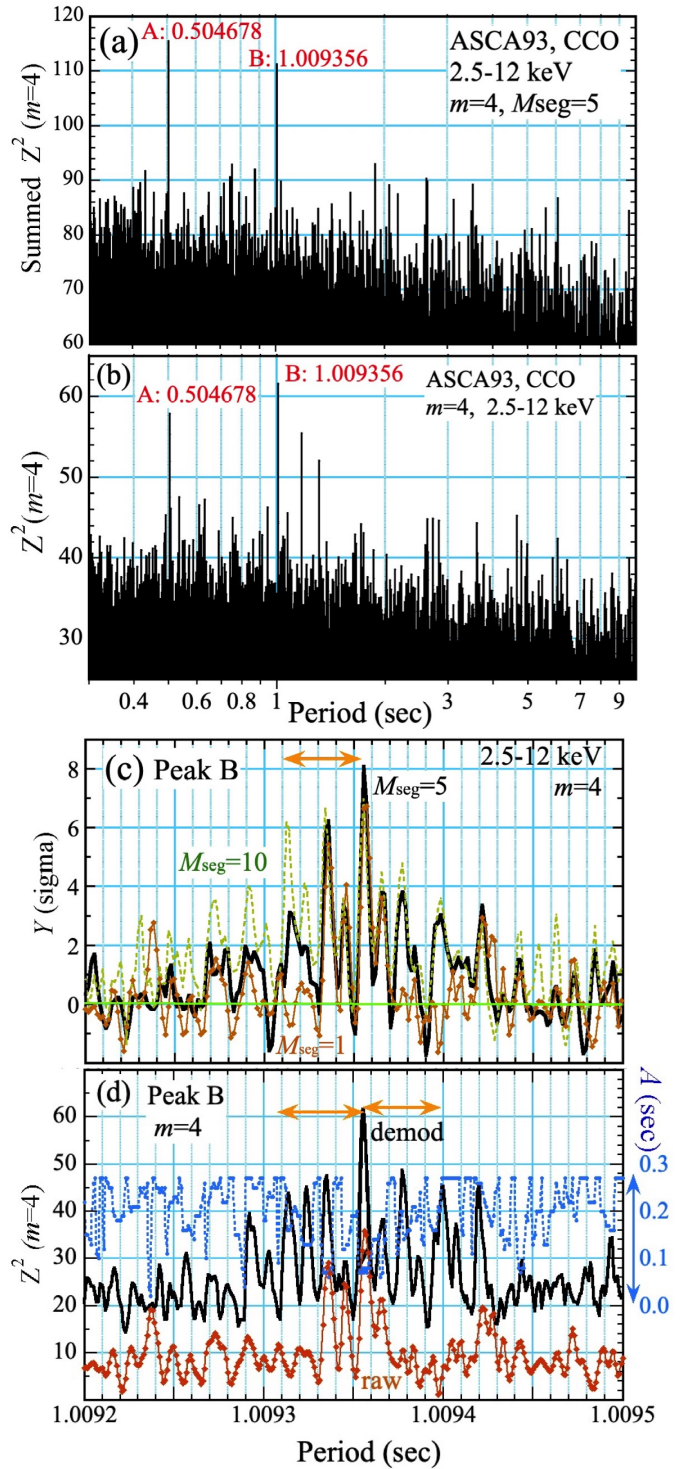


Fig. 2. (a) A phase-sorted PG for 2.5–12 keV CCO photons in ASCA93, calculated employing $m = 4$ and $M_{\text{seg}} = 5$. The 10–30 s region is truncated. (b) Same, but derived using the demodulation method assuming $T = 24.0$ ks. (c) Details of the PG in (a) around Peak B. Results with $M_{\text{seg}} = 1$ (brown with dots), 5 (solid black), and 10 (dashed green) are overlaid. The ordinate refers to equation (4). A horizontal arrow shows the expected fringe separation. (d) Details of the PG in (c) around Peak B. The amplitude A is shown in dashed blue (right ordinate). The dotted brown curve labeled “raw” is the result before demodulation. Alt Text: Four periodograms of 1E 1613 obtained with ASCA, in photon energies of 2.5 to 12 kilo-electronvolts. Top two cover the 0.3 to 30 second period range, whereas bottom two are their expanded views.

Gaussian case of 1.28×10^{-12} . This provides a good lesson that quoting a probability in “sigmas” is meaningless, unless the underlying probability distribution is rigorously specified.

To reconfirm the above argument, the periods of equations (3a) and (3b) actually appear, in the raw PG ($M_{\text{seg}} = 1$) with $m = 4$, as local peaks with $Z_4^2 \approx 31$ and $Z_4^2 \approx 36$, respectively. However, when plotted over wider period ranges, they become exceeded by many noise peaks. The phase-sorted analysis has made the two peaks far more outstanding, by mitigating the PPM disturbance working on them, and averaging out the noise peaks.

In figure 2c, we observe clear side lobe fringes. While those in the PGs with $M_{\text{seg}} = 5$ and $M_{\text{seg}} = 10$ can be readily ascribed to the beat between the artificial data gaps repeating with T (see orange arrows) or $2T$, those in the $M_{\text{seg}} = 1$ result (the raw PG) is somewhat puzzling, because the artificial data gaps are absent, and the flux is not strongly modulated at T . Probably, the $M_{\text{seg}} = 1$ side lobes are produced because the pulse fraction is actually modulated mildly at 24.0 ks.

3.3.3 Demodulation analysis

The results in figure 2a could be some artifacts specific to our new analysis tool. We hence cross checked them by a different tool, called “demodulation analysis”. It was first devised by Makishima et al. (2014) to search Suzaku data of a magnetar for the PPM period T , given the pulse period P . By modifying the logic, we here assume that an *unknown* fast pulsation in the data suffers the PPM at a *known* long period T of equation (1). Then, the arrival time t of each photon (including background) is modified to $t - \Delta t$, using a formula

$$\Delta t = A \sin(2\pi t/T - \psi_0), \quad (5)$$

where $A \geq 0$ is an assumed modulation amplitude, and ψ_0 (0 to 2π) is the phase of the first photon. This Δt means a correction of the pulse arrival time for delays (or advances if $\Delta t < 0$), relative to the case of precisely constant periodicity. Then, a “demodulated PG” is computed as before over a certain period interval, but at each P , we maximize Z_m^2 by scanning A and ψ_0 over appropriate ranges. We fix $T = 24.0$ ks, unless otherwise stated. A significant increase of Z_m^2 at a certain P would be regarded as a pulse candidate.

Compared to the phase-sorted PG (subsubsection 3.3.2), two advantages of this method are that we can recover full pulse-phase coherence among all photons, and the method has afforded the detections of free precession from the seven magnetars altogether (Makishima et al. 2024b). On the other hand, its clear disadvantage is the required much longer computational time.

Using the 2.5–12 keV energy interval which was found optimum in subsubsection 3.3.2, together with $m = 4$ and $\eta = 5$, we computed a demodulated PG over the same period interval. We fixed $T = 24.0$ ks, scanned A from 0 to $\approx P/4$ (a plausible maximum; Makishima et al. 2016) typically in 10 steps, and ψ_0 from 0 to 360° with 10° step. The obtained PG is shown in figure 2b, where a few outstanding peaks are seen. Of them, the highest two reproduce, within $\approx 1 \mu\text{s}$, equations (3a) and (3b) found in panel (a), although their relative heights have reversed. The derived modulation parameters are summarized in table 2. The two peaks demand nearly the same set of (A, ψ_0) , suggesting them to have a common origin. Thus, our results from the phase-sorted PGs have been reconfirmed and reinforced. For reference, a peak with $Z_4^2 \approx 40.1$ is observed also at $P_{93}/4$.

An expanded view of figure 2b is given in panel (d). It is very similar to (c), still showing the interference structure, even though the data are now free from the 24 ks data gaps, and the flux is not

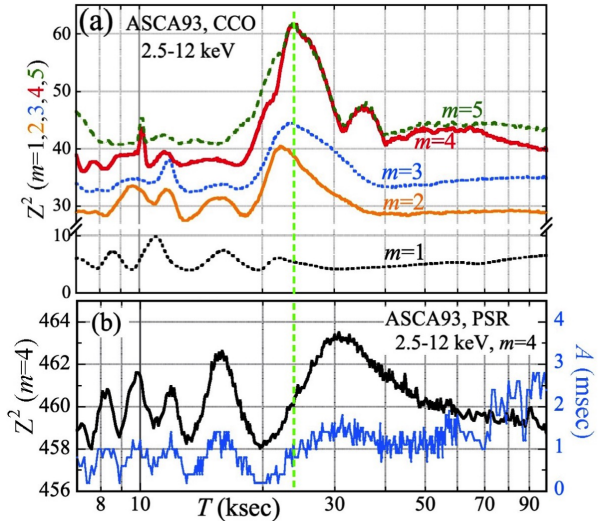


Fig. 3. (a) Demodulated Z_m^2 values from the ASCA93 CCO data in 2.5–12 keV, calculated with different m and shown against the assumed value of T . The pulse period is constrained to a vicinity of P_{93} . (b) A control study using the 69 ms pulsar in ASCA93, in the same energy range. The optimum value of A is shown in the lower trace (blue), using the right ordinate. Alt Text: Top panel shows the significance of the 1.01 second pulsation with ASCA, as a function of the modulation period from 7 to 100 kilo-seconds. Bottom panel is a control study using the 69 millisecond pulsar.

strongly modulated at this period. Again, this behavior is possibly due to the 24 ks variation of the pulse fraction, which we found to amount to a factor of ~ 2 . The dashed blue trace gives the values of A that maximize Z_4^2 . Also shown is the PG before demodulation, which is identical to the $M_{\text{seg}} = 1$ result in panel (c) except the difference in the ordinate variable.

3.3.4 Statistical significance of the ~ 1.01 s periodicity

A vital question is the statistical significance of the ~ 1.01 s periodicity. We carried out its evaluation, using the highest Peak B with $Z_4^2 = 61.5$ in the demodulated PG of figure 2d. As detailed in Appendix 1, the probability for a peak with $Z_4^2 \geq 61.5$ to appear by chance fluctuations, *at a given period* in this PG, was found to be $\mathcal{P}_{\text{ch}}^{(1)}(P_{93}) \approx 1.3 \times 10^{-8}$. When the trial number in the period search is multiplied, we obtain a post-trial probability of $\mathcal{P}_{\text{ch}}(P_{93}) \approx 0.54\%$ (see Appendix 1). This means a chance probability of finding $Z_4^2 \geq 61.5$ *at any period* from 0.3 s to 30 s. We regard this as a representative value for ASCA93, and list it in table 2. As a working hypothesis, hereafter we regard P_{93} as the spin period of 1E 1613 as of 1993 August. For reference, a comparable value of \mathcal{P}_{ch} is derived for the Peak A in the phase-sorted PG.

3.3.5 An independent determination of T

To reinforce the results derived so far, we carried out yet another effort. The present analysis is an attempt to search a region on the (P, T) plane for the highest Z_4^2 peak. The PGs in figure 2 provide cross sections of this peak along the P axis, in which $T = 24.0$ ks is pre-specified. We may alternatively compute a cross section along the T dimension, with $P \approx P_{93}$ fixed. So, we computed Z_m^2 incorporating equation (5), as a function of T rather than P , changing T in the same manner as equation (2). At each T , we maximized Z_m^2 , allowing P to float by $\pm 2 \mu\text{s}$ around P_{93} , and scanning A and ψ_0 in the same manner as before.

When applied to the 2.5–12 keV CCO data from ASCA93, this analysis yielded figure 3a, where results with $m = 1$ through $m = 5$

Table 2. Results of the demodulation analysis of 1E 161348–5055 using $m = 4$.

Data	time 0*	Energy range	P (s)	Z_4^2	A (s)	ψ_0	$\mathcal{P}_{\text{ch}}^{(1)\dagger}$	$\mathcal{P}_{\text{ch}}^{\dagger}$	PF [‡]
ASCA93	49216.9211	2.5–12 keV	$1.0093558(8) = P_{93}$	61.5	0.08	40°	1.3×10^{-8}	0.54%	0.16
XMM01	52155.8016	2.7–10 keV	$1.0096311(70) = P_{01}$	44.2	0.24	40°	1.2×10^{-5}	0.92%	0.14
XMM05	53605.3177	1.4–10 keV	$1.0097713(6) = P_{05}$	47.2	0.28	350°	1.1×10^{-5}	19%	0.07
XMM16	57619.7342	6.6–12 keV	$1.0101518(12) = P_{16}^X$	47.7	0.25	290°	9×10^{-6}	11%	0.25
NuS16	57563.6136	11–60 keV	$1.0101480(7) = P_{16}^N$	56.9	0.20	140°	— [§]	— [§]	0.30
		3–6 keV	$1.0101479(9) = P_{16}^N$	49.0	0.29	0°	— [§]	— [§]	0.09
NuS17	57906.3899	5.1–12 keV	$1.0101794(10) = P_{17}$	48.6	0.20	10°	— [§]	— [§]	0.24

* MJD of the first photon in the data.

† $\mathcal{P}_{\text{ch}}^{(1)}$ and \mathcal{P}_{ch} are pre- and post-trial probabilities, respectively. The ASCA93 results refer to Peak B in the demodulated PG and the period search range of 0.3–30 s. \mathcal{P}_{ch} of the other data sets are calculated against equation (7).

‡ The pulse fraction defined in subsubsection 3.4.2.

§ Not evaluated due to technical difficulties (see text).

|| Derived using only a limited interval of the modulation phase.

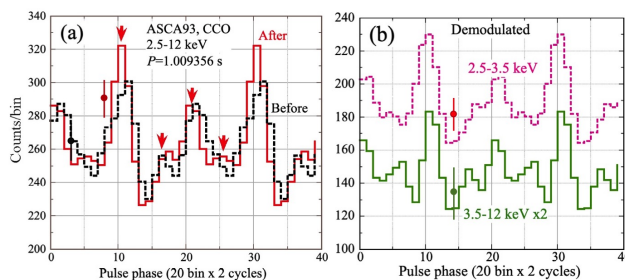


Fig. 4. Pulse profiles of 1E 1613 in ASCA93. (a) Results in 2.5–12 keV folded at P_{93} , before (dashed black) and after (solid red) the demodulation using $T = 24.0$ ks. (b) Demodulated pulse profiles in the 2.5–3.0 keV and 3.5–12 keV energy ranges. Alt Text: Folded pulse profiles with ASCA.

are shown together. For $m = 3$ to 5, the pulse significance indeed becomes maximum at $T \approx 24$ ks, or more specifically at

$$T = 23.8^{+3.2}_{-1.5} \text{ ks } (m = 4). \quad (6)$$

This peak has a relative enhancement by $\Delta Z_4^2 \sim 20$ above the surroundings, and the probability for this increment to take place by chance is estimated as $\exp(-\Delta Z_4^2/2) \approx 4.5 \times 10^{-5}$ (Makishima et al. 2023). After considering the effective number of trials in T , about 40, the probability still remains at $\approx 0.2\%$. The peak is hence statistically significant. Solely via timing studies, we have thus arrived at an estimate of T that is consistent with equation (1), even though the 24 ks flux variation of 1E 1613 is unclear in ASCA93.

The ~ 1.01 s periodicity could be some instrumental artifacts of either ASCA or the GIS, rather than specific to 1E 1613. We hence applied the same analysis to the ASCA93 data of the ideal reference, the 69 ms pulsar, and computed its demodulated Z_4^2 as a function of T . To reproduce the condition for 1E 1613, the energy range was changed from the original 3–10 keV to 2.5–12 keV, and the harmonic number from $m = 2$ (figure 1) to $m = 4$.

The derived T -dependence of Z_4^2 of the pulsar is presented in figure 3b. Although some oscillatory behavior is seen, Z_4^2 remains mostly within $\sim \pm 4.72$ (68% error associated with a peak value) of the average at ~ 461 . In particular, no enhancement is seen at $T = 24$ ks. Also, the modulation amplitude remains $A < 3$ ms, or $< 0.043P$. We conclude that the 69 ms pulsar signal is free from PPD at any period between $T = 7.0$ and 100 ks, including 24.0 ks.

3.3.6 Pulse profiles

When evaluating a candidate periodicity, folded pulse profiles provide important information. Figure 4a shows 2.5–12 keV pulse profiles of 1E 1613 in ASCA93, before (dashed black) and after (solid red) the demodulation, which employs equation (5) and the parameters in table 2. Both are folded at P_{93} , and smoothed with a running average which combines three adjacent bins (e.g., Makishima et al. 2021a). As a result, the error associated with each data bin is 0.61 times the Poissonian value. The profiles are both double-peaked, with a larger main peak and a smaller sub peak.

The demodulation is seen to make the main peak higher, and enhance fine structures in the profile. As a result, the demodulated profile acquires a clear 4-peak structure, as indicated by four downward arrows (in red). This reinforces the pulse reality, because similar 4-peak structures are rather common to magnetars (Makishima et al. 2019, 2021ab, 2024a), even though its interpretation is still an open question.

When the Fourier power of the demodulated profile in figure 4a is summed up to the 4th harmonic, the result gives the P_{93} peak height, $Z_4^2 = 61.5$. It is contributed by individual harmonic, from the fundamental to the 4th harmonic, by 6.7%, 53.2%, 10.0%, and 30.1%, respectively. Thus, the second harmonic is dominant, in agreement with the double-peaked pulse profile, and the strong 2nd harmonic signal emerging in panels (a) and (b) of figure 2. The 4th harmonic gives the second strongest contribution.

In figure 4b, the pulse profiles were derived in a softer (2.5–3.5 keV) and a harder (3.5–12 keV) energy intervals, both demodulated under the same condition as the red profile in panel (a). They are very much alike, except that the hard-band profile exhibits a sharper main peak and a more prominent 4-peak structure. This energy dependence is similar to the case of the magnetar SGR 1900+14 (Makishima et al. 2021b).

3.4 XMM-Newton data in 2001 (XMM01)

To reinforce the evidence from ASCA93 for the ~ 1.01 s pulsation of 1E 1613, we proceed to the analysis of XMM01. We then need to redefine the period search range, using some assumptions on \dot{P} . As a simple way, we may assume that the characteristic age of 1E 1613, $\tau_c \equiv P/2\dot{P}$, should be comparable to the age of the host SNR, 2.0–4.4 ky (Carter et al. 2019; Braun et al. 2019). Selecting the shorter of the two, we obtain a nominal spin-down rate as $\dot{P} = 7.9 \times 10^{-12} \text{ s s}^{-1}$. To be conservative, let us allow a ~ 2.5 times larger value, $\dot{P} \sim 2.0 \times 10^{-11} \text{ s s}^{-1}$, as an upper

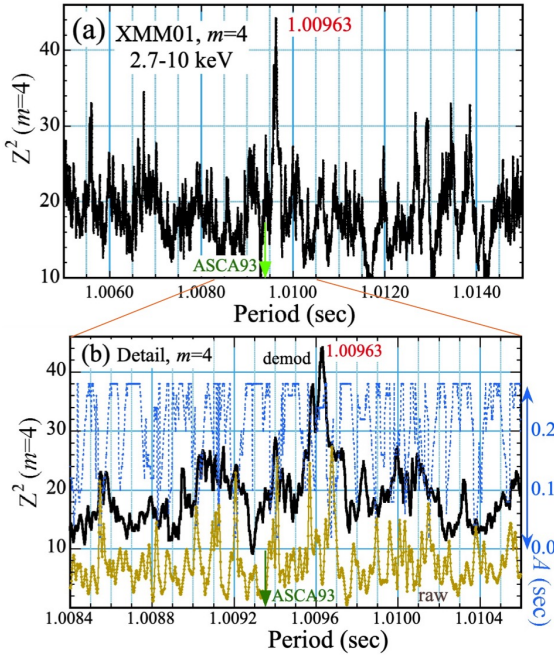


Fig. 5. Results on 1E 1613 from the 2.7–10 keV XMM01 data. (a) A de-modulated PG with $m = 4$, derived in the same way as figure 2b but over a more limited period range of equation (7). The downward arrow indicates P_{93} . (b) An expanded view (in solid black) of panel (a) around the peak, and the optimum A in dotted blue (right ordinate). The $m = 4$ PG before the demodulation (labeled “raw”) is superposed as an ochre line. Alt Text: Periodograms with XMM-Newton in 2001, in 2.7 to 10 kilo-electronvolts.

limit. This implies a spin down by $\Delta P \sim 5$ ms in 8 yrs from ASCA93 to XMM01. Hence, we set the longest limit of the period search at 1.015 s. The shortest limit will be somewhat arbitrarily set at 1.005 s, even though the case of $P < P_{93}$ is unphysical. The selected period search range, hereafter called a *fiducial interval*, becomes approximately symmetric around P_{93} as

$$P = 1.005 - 1.015 \text{ s.} \quad (7)$$

3.4.1 PGs from XMM01

Over the fiducial period interval, we calculated a raw PG from XMM01. After ASCA93, the 2.5–10 keV band was used, together with $m = 4$. For the reason described in subsection 2.3, E_U was set at 10 keV rather than 12 keV. However, no significant peak exceeding $Z_4^2 \sim 35$ was found.

We hence incorporated the demodulation with equation (5), because the XMM01 data are too short to analyze with the phase-sorted technique. We again fixed $T = 24.0$ ks. Then, in the PG, a dominant peak with $Z_4^2 = 41.3$ has appeared at a period

$$P = 1.0096311(70) \text{ s} \equiv P_{01}, \quad (8)$$

which is longer than P_{93} by $\Delta P = 0.275$ ms. As shown in figure 5a, the peak became higher to $Z_4^2 = 44.2$ (with P unchanged), when E_L is raised from 2.5 keV to 2.7 keV. Details around the peak is shown in figure 5b, together with some additional information, while relevant parameters are given in table 2. The peak width ($\sim 70 \mu$ s) is much larger than that of P_{93} ($\sim 6 \mu$ s), because of the short length of XMM01.

In Appendix 1, we examined the statistical significance of this periodicity, in the same way as for ASCA93. Then, it was found to have $\mathcal{P}_{\text{ch}}(P_{01}) \approx 0.92\%$ (table 2), when evaluated over the fiducial period interval, and considering trials in P and E_L (but not in m because we tried $m = 4$ only). Hence, the signal at P_{01} is likely to

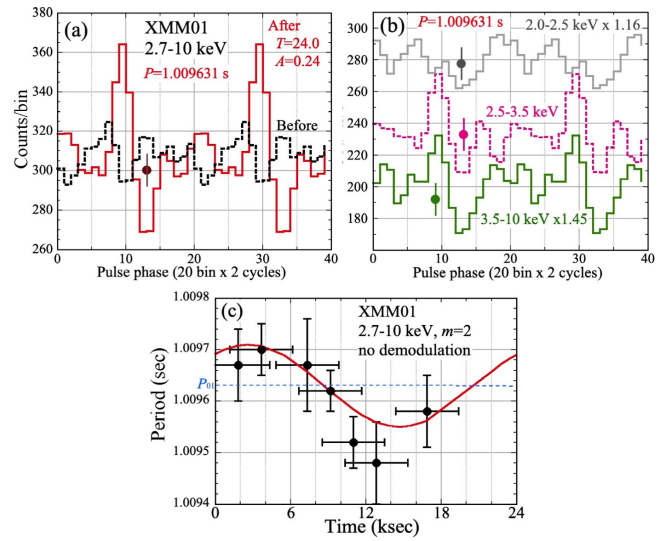


Fig. 6. (a) XMM01 pulse profiles in 2.7–10 keV, folded at P_{01} and shown in the same way as figure 4a. (b) Pulse profiles at P_{01} derived in three energy ranges. (c) Instantaneous pulse periods in XMM01 determined with $m = 2$ in 2.7–10 keV, without demodulation, shown against the elapsed time from the data start. The solid red curve is a prediction by the optimum modulation parameters, and the dashed horizontal line indicates P_{01} . Alt Text: Folded pulse profiles from XMM-Newton in 2001. The bottom panel shows instantaneous pulse periods without demodulation.

be real as well, and to represent the object’s pulse period in 2001. We are then allowed to connect P_{93} with this P_{01} , to derive

$$\dot{P} = (1.09 \pm 0.04) \times 10^{-12} \text{ s s}^{-1} \quad (9)$$

which is reasonable for a young pulsar (see subsection 4.4).

3.4.2 Pulse profiles from XMM01

The demodulated 2.7–10 keV pulse profile of XMM01, shown in solid red in figure 6a, is amazingly similar to that with ASCA93 (figure 4a). Also similar is the pulse fraction, defined as $\frac{1}{2}(\text{maximum} - \text{minimum})/\text{average}$, which is 0.16 for ASCA93 and 0.14 for XMM01 (table 2). These support that P_{93} and P_{01} represent the same phenomenon, i.e., the fast rotation of the NS in 1E 1613. As a difference, the raw profile in XMM01 is more strongly suppressed than that in ASCA93. This is because the modulation amplitude, $A \approx 0.08$ s in ASCA93, increased to $A \approx 0.24$ s in XMM01 (table 2), which is close to the upper limit, $A \approx P/4$. Such a change in A is not rare among magnetars (Makishima et al. 2019).

Figure 6b presents energy-sorted pulse profiles in XMM01, all folded at P_{01} using the same set of (A, ψ_0) . The 2.5–3.5 and 3.5–10 keV results again look alike, but the 2.0–2.5 keV profile is considerably different. This is also evidenced by the P_{01} peak height in the PG, which decreases as E_L is lowered from 2.5 keV downward. Thus, some changes in the pulse properties are suggested at < 2.5 keV. This information was unavailable with the SNR-contaminated ASCA data.

Utilizing the high CCO flux in XMM01, together with the large effective area of XMM-Newton, we time-divided the data into overlapping ten segments. From each of them, we calculated a 2.7–10 keV PG, *without demodulation* and using $m = 2$. Because the PPM effect is mild within each segment, seven out of the ten PGs showed clear peaks at $\sim P_{01}$. We were hence able to determine the instantaneous pulse periods as shown in figure 6c. These periods are consistent with the solid curve in red, which is predicted by (A, ψ_0) in table 2. The two turning points of this curve

are confirmed, in the “raw” PG in figure 5b, as a pair of horn-like features on both sides of P_{01} . These non-trivial properties of P_{01} strengthen its association with the 6.67 hr periodicity.

3.5 XMM-Newton data in 2005 (XMM05)

Let us next analyze XMM05, hoping to find a periodicity that is consistent with P_{93} and P_{01} . In this observation, 1E 1613 was about 4 times fainter than in XMM01 (table 1), but this may be compensated for by the ~ 4 times longer exposure of XMM05. On this occasion, 1E 1613 exhibited the 24.0 ks flux variation clearly, with a rather sinusoidal waveform (DL06).

3.5.1 PGs from XMM05

If the fast pulsation of 1E 1613 has a constant \dot{P} as in equation (9), the pulse period in XMM05 is predicted, from P_{93} and P_{01} , as

$$\text{XMM05} : P = 1.009769(15) \text{ s.} \quad (10)$$

The constant- \dot{P} assumption, however, may not necessarily be warranted. Therefore, we retained the fiducial search interval [equation (7)] used for XMM01, and calculated an $m = 4$ PG in 2.5–10 keV. Since no outstanding periodicity was seen therein, we next incorporated the demodulation correction, keeping the same period and energy regions. Considering the long data span, T was allowed to vary from 23.8 to 24.2 ks. The demodulated PG showed several peaks up to $Z_4^2 \sim 45$, but none of them was dominant, and none fell in or close to the error range of equation (10).

We repeated the demodulation, keeping $E_U = 10$ keV, but this time changing E_L both above and below 2.5 keV. (Although the pulsation in XMM01 was suppressed for $E_L < 2.5$ keV, the pulse properties may have changed as the flux decreased.) As E_L is lowered from 1.6 keV downwards, a dominant peak has emerged in the PG, and its height became maximum at $E_L = 1.4$ keV. The demodulated $m = 4$ PG under this condition is presented in figure 7a, where the periodicity appears as the highest peak at

$$P = 1.0097713(6) \text{ s} \equiv P_{05}. \quad (11)$$

Because this P_{05} falls right on the prediction of equation (10), we may identify it with the source pulsation. This also suggests that \dot{P} is rather constant, and updates equation (9) to

$$\dot{P} = 1.097(4) \times 10^{-12} \text{ s s}^{-1}. \quad (12)$$

Figure 7b gives details of figure 7a around the peak. Shown together are results from two other conditions; one with the same $E_L = 1.4$ keV but without demodulation (labeled “raw”), and the other with the demodulation but using $E_L = 1.7$ keV. Thus, the pulse detection from 1E 1613 requires not only the demodulation correction with equation (5), but also a selection of an appropriate E_L , possibly depending on the data set. While the decrease of Z_4^2 for $E_L \gtrsim 1.6$ keV is due likely to a decrease of the signal photons, that toward $E_L < 1.4$ keV could be intrinsic.

We also calculated the Z_4^2 value as a function of T , and show the result in figure 7c, in a similar way to figure 3a. The $T = 24.0$ ks peak is reproduced very clearly, at 23.9 ± 0.3 ks, and more sharply because of the larger amplitude, $A \approx 0.28$ in XMM05, than $A \approx 0.08$ in ASCA93. Also, the optimum P is seen to converge to P_{05} ; the Z_4^2 peak is hence confined to a well-defined region on the (P, T) plane.

The chance probability of the P_{05} peak in figure 7a is rather modest, $\mathcal{P}_{\text{ch}}(P_{05}) \approx 19\%$ (Appendix 1), if we count all period trials in the interval of figure 7a, together with those in E_L . However, it decreases to $\mathcal{P}_{\text{ch}}(P_{05}) \approx 0.2\%$ when N_{trial}^P is calculated over the period range of figure 7b. Since this range fully accommodates the prediction from P_{93} and P_{01} , we consider that the XMM05 data have provided another detection of the 1.01 s pulse period.

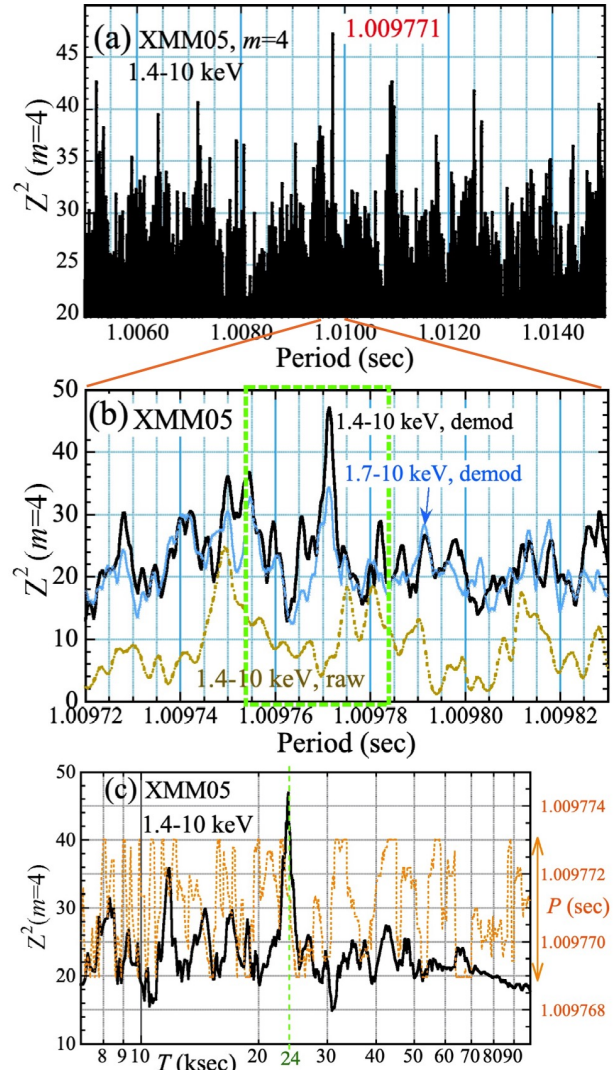


Fig. 7. Results from XMM05. (a) A demodulated $m = 4$ PG, in 1.4–10 keV. (b) Details of (a), together with a result in 1.7–10 keV (thin cyan), and the 1.4–10 keV “raw” PG (in ochre). A green box indicates the prediction of equation (10). (c) Values of Z_4^2 in 1.4–10 keV, shown against T . A dashed orange curve is the optimum P . Alt Text: Periodograms with XMM-Newton in 2005, in photon energies of 1.4 to 10 kilo-electronvolt. Bottom panel shows the pulse significance against the modulation period.

3.5.2 Pulse properties in XMM05

When folded at P_{05} , the 1.4–10 keV XMM05 data yielded pulse profiles shown in figure 8a. The demodulated profile reveals the 4-peak structure very clearly. (To resolve the fine structure, here one pulse cycle is divided into 28 bins, instead of 20). This profile is contributed by the fundamental to the 4th harmonic, by 19.7%, 18.4%, 8.7%, and 53.2%, respectively. Thus, in contrast to the dominance of the 2nd harmonic in the profile of ASCA93 (and of XMM01), now the 4th harmonic becomes dominant.

Figure 8b shows energy dependence of the demodulated pulse profile. The 4-peak feature, seen in 1.4–2.5 keV, changes into a 3-peak structure in 2.5–10 keV, whereas it splits into finer peaks below 1.4 keV; this may explain the decrease of the peak Z_4^2 for $E_L < 1.4$ keV.

The XMM05 results provide not only an additional support to the pulse reality, but also several pieces of valuable information. The inset to figure 8c is the 1.4–10 keV photon counts folded at 23.9 ks (maximizing the PG peak), which reconfirms the reported

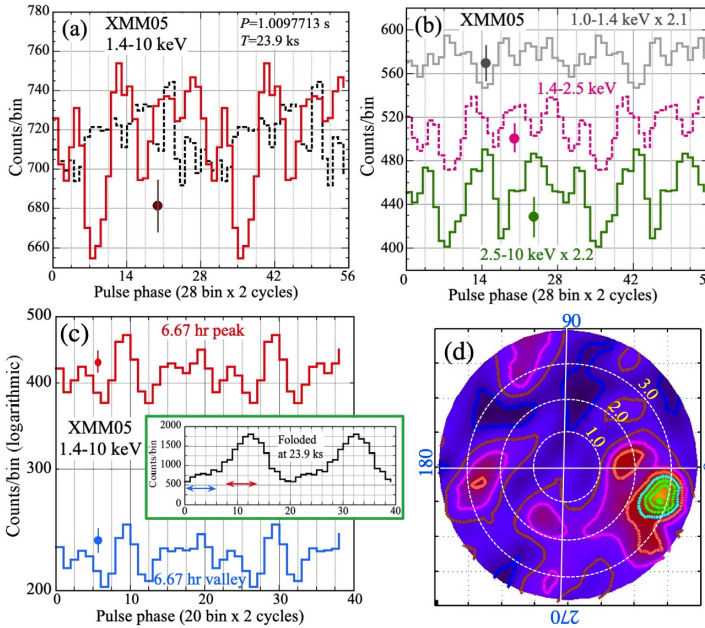


Fig. 8. (a) Pulse profiles from XMM05 in 1.4–10 keV, folded at P_{05} into 28 bins. (b) Same, but derived in three separate energies. (c) Same as (a), but the profiles are accumulated over the peak (top in red) and valley (bottom in blue) phases of the 6.67 hr cycle. The 1.4–10 keV counts folded at 23.9 ks are shown in the inset. (d) Values of Z_4^2 in XMM05, shown on the (A, ψ_0) polar plane. They are derived with demodulation using $T = 23.9$ ks and $P = P_{05}$. Alt text: Some properties of the pulsation of 1E 1613, in the 2005 XMM-Newton data.

flux modulation (DL06). When the photons are accumulated over the peak and valley phases of the cycle as indicated by two arrows, we obtain the demodulated pulse profiles shown at the top (in red) and bottom (in blue) of figure 8c, respectively. Here, the ordinate is logarithmic to enable a direct comparison of the two profiles. Between the two modulation phases, neither the pulse profile nor the pulse fraction differs significantly.

As in the figure 8c inset, the 6.67 hr flux variation in XMM05 happens to be close to the minimum at $t = 0$. Then, at this epoch, how is the pulse-timing lag Δt in equation (5) behaving? For this purpose, figure 8d shows the values of Z_4^2 as a contour plot on a (A, ψ_0) polar plane, where $P = P_{05}$ and $T = 23.9$ ks are fixed. Thus, the demodulation solution is constrained to $A \approx 0.28$ s and $\psi_0 \approx 350^\circ$. The pulse-phase lag is hence close to zero at $t = 0$, and is increasing with time. This result fits very naturally into the possible emission geometry presented in subsection 4.3.

3.6 XMM-Newton data in 2016 (XMM16)

The primary aim of analyzing XMM16 is to find another piece of evidence for the 1.01 s pulsation. A successful detection would be followed by two more aims; to refine the knowledge on \dot{P} (e.g., its constancy) utilizing the time span from XMM05, and to look for possible effects of the 2016 June episode. We must be cautious that the pulse properties may change across ~ 5 keV, as suggested by the two-band light curves in figure 9a, which reconfirm figure 4 of Esposito et al. (2019). To enhance the information above ~ 5 keV, we raise E_U from 10 keV to 12 keV.

Assuming that \dot{P} of the source is constant at equation (12), the pulse period in XMM16 is predicted as

$$\text{XMM16} : P = 1.010151(2) \text{ s} \quad (13)$$

where the uncertainty is already dominated by those in P rather

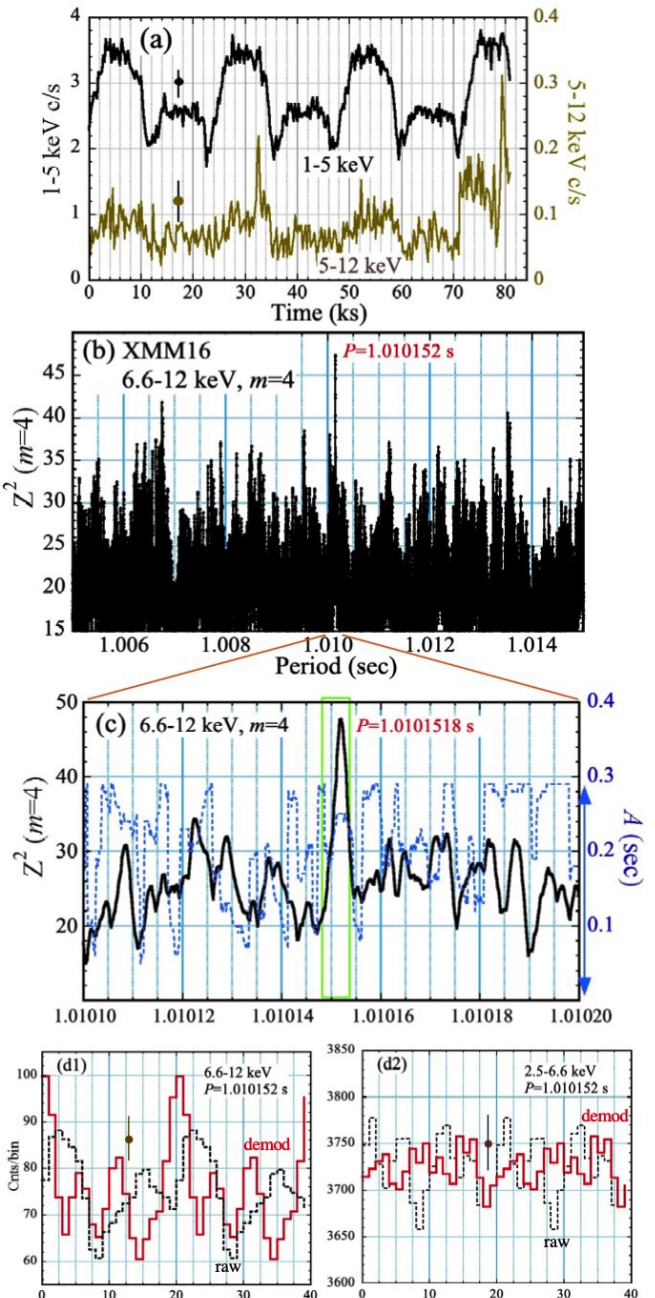


Fig. 9. Results from XMM16. (a) Light curves in 1–5 keV (left ordinate) and 5–12 keV (right ordinate), with 250 s binning. (b) A demodulated 6.6–12 keV PG with $m = 4$. (c) Details of (b), where the green box indicates equation (13). (d1) Pulse profiles in 6.6–12 keV folded at P_{16}^X , before (dashed black) and after (solid red) the demodulation. (d2) Same as (d1), but in 2.5–6.6 keV. The demodulation uses the same parameters as for (d1). Alt Text: Results on 1E 1613 from the XMM-Newton data in 2016. Top panel shows two-band light curves with 250 second binning. Next two graphs are periodograms, and the bottom two give folded pulse profiles in two energy ranges.

than \dot{P} . However, considering again possible changes in \dot{P} , over 11 yrs an/or across the brightening episode, we retained the fiducial period-search range of equation (7), and computed simple PGs in various energy ranges above and below 5 keV. No noticeable periodicity was found, just as in the preceding three data sets.

We then applied the demodulation to the data, using $m = 4$ and $E_U = 12$ keV. The search failed for $E_L \lesssim 6$ keV, as each PG showed multiple peaks with similar heights (typically $Z_4^2 \lesssim 38$). In contrast, PGs with $E_L \gtrsim 6$ keV revealed a unique candidate, which became most prominent ($Z_4^2 \approx 47.7$) at $E_L = 6.6$ keV. The result is shown in panels (b) and (c) of figure 9, where the candidate stands out at

$$P = 1.0101518(12) \text{ s} \equiv P_{16}^X. \quad (14)$$

As described in Appendix 1, this peak is estimated to have $\mathcal{P}_{\text{ch}}^{(1)}(P_{16}^X) \approx 9 \times 10^{-6}$, and $\mathcal{P}_{\text{ch}}(P_{16}^X) \approx 11\%$, when we consider trials in P over equation (7), plus those in E_L . Although this result is modest, the peak remains the highest over the entire interval of equation (7), and yet falling right on the prediction of equation (13). As a result, $\mathcal{P}_{\text{ch}}(P_{16}^X)$ decreases to 0.1%, just as we found with XMM05, when N_{trial}^P is calculated over the period range of figure 9c. It further decreases to 0.04%, if calculated against the predicted period uncertainty of equation (13). Therefore, P_{16}^X is again likely to be a real pulse period. In addition, the constancy of \dot{P} at equation (12) has been reinforced.

Pulse profiles from XMM16, in 6.6–12 keV and 2.5–6.6 keV, are given in panels (d1) and (d2) of figure 9, respectively. The demodulated 6.6–12 keV profile is similar to those in ASCA93 and XMM01, reinforcing the reality of P_{16}^X . In contrast, the low-energy folded profiles in (d2) are much featureless, regardless of the demodulation correction; the pulse fraction, if any, is at most $\sim 1/30$ of that in (d1). These low-energy properties did not change even when allowing (A, ψ_0) to take different values from those in 6.6–12 keV. These results reconfirm the apparent failure in detecting the pulsation below 6.6 keV.

Then, what is taking place in the softer energies? The pulses must be present there as well, because the emission should not become suddenly isotropic at < 6 keV. At the same time, the PPM must also be operating, because otherwise the pulse would be directly visible. A likely scenario to explain these conditions is presented in subsubsection 4.5.2.

As anticipated in advance (subsection 2.3), the pulse detection in XMM16 was less straightforward than in the preceding three data sets, mainly due to complex pulse behavior in < 6 keV where most of the photons are present. This may possibly due, in turn, to the source activation 2 months before. Nevertheless, the ~ 1.01 s pulsation has been reconfirmed in XMM16 as well, and \dot{P} has been found to be quite constant for 23 yrs from 1993 to 2016, with no precursory changes preceding the activation episode.

3.7 NuSTAR data in 2016 (NuS16)

In an attempt to obtain the pulse information for the first time in hard X-rays above ~ 10 keV, we analyze the NuS16 data, keeping in mind the following reservations. (i) As described in subsection 2.1, the data were taken only 3 d after its activation on 2016 July 22. Therefore, an enhanced timing noise may be anticipated. (ii) Since the data were taken only 54 days before XMM16, equation (12) accurately predicts the pulse period to appear at $P = P_{16}^X - 5.1 \mu\text{s} \approx 1.010147$ s, unless short-term changes in P or \dot{P} took place. For the first-cut pulsation search, we hence select a narrower interval, $P = 1.0101 - 1.0102$ s. (iii) As described by Rea et al. (2016) and reconfirmed in figure 10a, the 6.67 hr

intensity variation on this occasion had a double-peaked profile, just as in XMM16. (iv) Like magnetars, the wide-band spectrum of 1E 1613 generally exhibits two-component nature (Rea et al. 2016), wherein a thermal-like soft component and a power-law like hard component cross over at ~ 10 keV. We hence analyze the data above and below 10 keV separately.

3.7.1 Hard X-ray results from NuS16

Simple PGs, either above or below 10 keV, did not yield convincing results. We thus proceed to the demodulation analysis, first in hard X-rays because the pulsation in XMM16 was less disturbed in harder energies. When using $E_L \gtrsim 10$ keV and $E_U = 45 - 70$ keV, the demodulated PGs consistently revealed a noticeable peak, at a period in agreement with the prediction. As shown in figure 10b by a solid black line, it reached the maximum of $Z_4^2 \approx 41$, for $E_L = 11$ keV and $E_U = 60$ keV. The secondary peak at $P \approx 1.010105$ s is its prograde beat between the $T = 24$ ks periodicity.

Although the hard X-ray data have thus provided evidence for the expected pulsation, the peak is not high enough, and is overwhelmed by other noise peaks when the PG is calculated over the fiducial interval of equation (7). Presumably, the NuS16 data take during the high activity violate the basic assumption behind equation (5), that all features in the pulse profile shift in parallel, and in a sinusoidal manner, throughout the modulation phase $[t/T]$.

Given the above possibility, we repeated the demodulation using only those photons that fall in a limited modulation phase³, between $[t/T]_1$ and $[t/T]_2$ ($0 \leq [t/T]_1 < [t/T]_2 \leq 2.0$) referring to panel (a). As shown in figure 10b by a red line with dots, the peak in the demodulated 11–60 keV PG became much higher, reaching $Z_4^2 = 56.9$, when $[t/T]_1 = 0.52$ and $[t/T]_2 = 1.08$ are chosen. The main peak position has remained the same, and is given as

$$P = 1.0101480(7) \equiv P_{16}^N, \quad (15)$$

which agrees well with the prediction from P_{16}^X . The peak disappears (dashed cyan curve in figure 10b) when the complementary modulation phase, $0.08 - 0.52$, is used. Details of the modulation-phase dependence are given in Appendix 2.

In figure 10c, we calculated the demodulated PG, using the same energy range and the same modulation phase (0.52–1.08), but reviving the period range of equation (7). There, the P_{16}^N peak still remains the highest, even though the number of period trials have increased by two orders of magnitude. This may provide some flavor as to the peak reality, although we skip calculating its statistical significance, because the effective trial number in choosing the modulation phase is difficult to estimate.

Folded pulse profiles in 11–60 keV are shown in figure 10d, for the conditions of the three PGs in panel (b). They are all demodulated with $A = 0.2$ s and $\psi_0 = 140^\circ$. The middle one (in red), using $[t/T] = 0.52 - 1.08$, yields $Z_4^2 = 56.9$, and exhibits a clear 3-peak structure. Among the three subpeaks, the highest one at a pulse-phase bin 8 disappears in the bottom (blue) profile which uses the complementary modulation phase, resulting in $Z_4^2 \approx 21$. The top profile (in black), with $Z_4^2 \approx 41$, is for the total modulation phase. We now understand the reason why the demodulation was most successful when using $[t/T] = 0.52 - 1.08$; outside this modulation phase, the brightest emission component becomes invisible, due, e.g., to self-eclipse, or deflection of the X-ray beam off our line-of-sight. This strong dependence on the modulation phase makes a contrast with figure 8c for XMM05, where two distinct modulation phases gave similar pulse profiles. Further information on this issue is provided in Appendix 2.

³ This is similar to the phase-sorted PG (subsubsection 3.3.2), but differs in that we focus on a single modulation-phase interval, and apply demodulation.

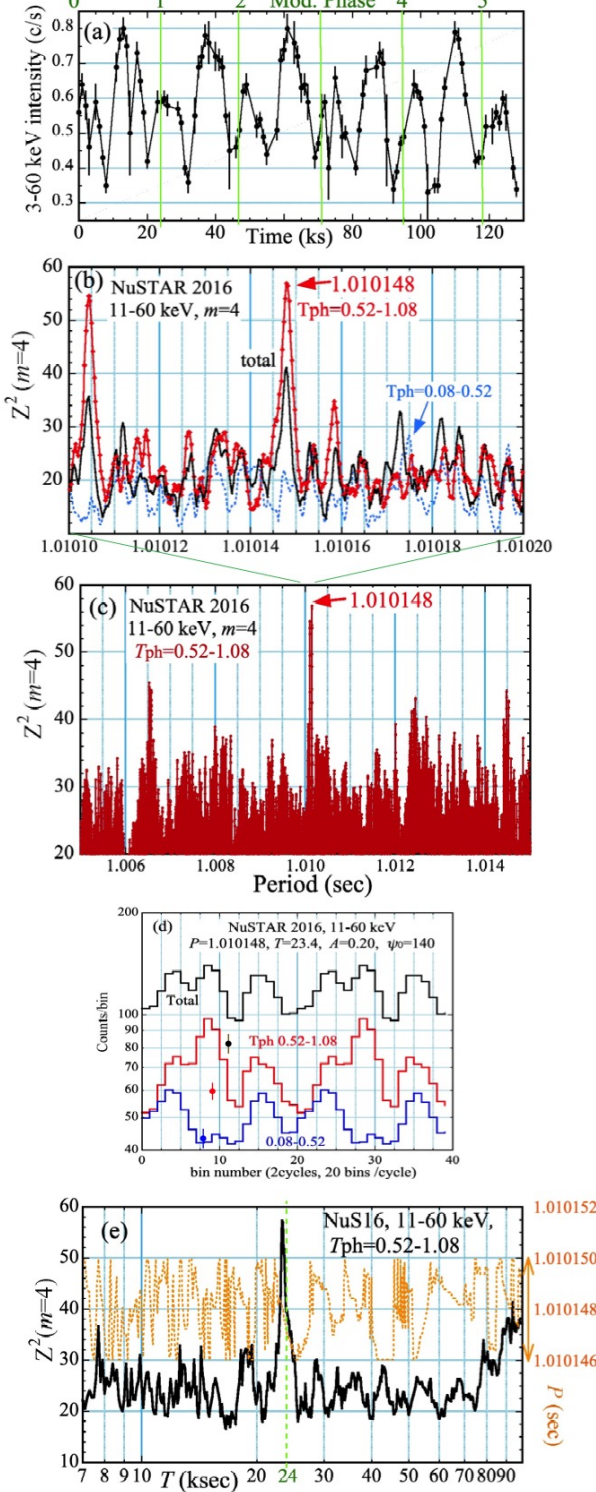


Fig. 10. Results from NuS16, mainly above 10 keV. (a) A background-inclusive 3–60 keV light curve from NuS16, with 1 ks binning. The modulation phase t/T , using $T = 23.4$ ks and the origin at the data start, is indicated in the top abscissa. (b) A demodulated 11–60 keV PG with $m = 4$ (solid black curve), presented over a narrow period range. The PGs for $[t/T] = 0.52 - 1.08$ and $0.08 - 0.52$ are given by a solid red curve with dots and a dashed cyan curve, respectively. (c) The same as the red curve in (b), but the period range is expanded to that of equation (7). (d) Pulse profiles in the three modulation-phase intervals (see text). (e) The Z_4^2 values shown as a function of T , calculated under the same condition as the red curve in (b), but limiting P to within $\pm 2 \mu\text{s}$ of $P = P_{16}^N$. Alt Text: Results from the 11–60 kilo-electronvolt data of NuSTAR in 2016. Shown are a light curve, two periodograms, three pulse profiles, and the pulse significance against the assumed modulation period.

As the last piece of hard-band information from NuS16, figure 10e presents how the pulse Z_4^2 derived via demodulation depends on the assumed T , just as in figure 3a and figure 7c. The solution indeed stands out, and gives a constraint as

$$T = 23.4 \pm 0.2 \text{ ks.} \quad (16)$$

This appears somewhat smaller than those from the other data sets; this issue is examined later in subsection 4.5.

3.7.2 Soft X-ray results from NuS16

The pulsation search was performed also in two soft X-ray bands of NuS16, 3–6 keV and 6–10 keV, which contain much larger number of background-inclusive photons, 31479 and 6431 respectively, than the 11–60 keV band (2367 photons). By changing $[t/T]_1$ and $[t/T]_2$, we searched for evidence of the pulsation.

In the 3–6 keV demodulation analysis, a choice of $[t/T] = 0.92 - 1.52$ (see Appendix 2 for details) yielded figure 11a, where the pulsation has been recovered exactly at P_{16}^N with $Z_4^2 = 49.0$, with several side lobes on both sides. While T of equation (16) is reconfirmed, the preferred modulation phase is nearly complementary to what was favored by the hard X-ray photons. The optimum modulation parameters (A and ψ_0 ; table 2) also differ from those in 11–60 keV. As shown in figure 11b, the peak remains the highest, even when the period range is expanded to equation (7).

Folded pulse profiles in 3–6 keV are presented in figure 11c, for $[t/T] = 0.92 - 1.52$ (solid line in red), and for $[t/T] = 0 - 1$ (total, in dashed black), with the latter scaled by 1/2. Both have been demodulated using the same parameters in table 2. The former profile is similar to those in ASCA93, XMM01, and XMM16, but the pulse fraction is ~ 0.09 , which is much lower than that in 11–60 keV (~ 0.3). The dominant peak, seen in the profile with the limited $[t/T]$, turns into a valley in the other one.

To assess the 11–60 keV vs. 3–6 keV consistency, we have incoherently summed up the PGs in figure 10c and figure 11b, ignoring their differences in the pulse profile, A , ψ_0 , and the $[t/T]$ interval. The result is presented in figure 11d, together with its details in the inset. Thus, the hard and soft peaks at P_{16}^N nicely add up to form an outstanding peak, accompanied by a series of side lobes on both sides due to the beat with $T = 24$ ks. This result provides visual evidence for the pulsation in NuS16.

We also analyzed the 6–10 keV photons from NuS16, by changing $[t/T]_1$ and $[t/T]_2$ in a similar way. However, no evidence for the pulsation at $\sim P_{16}^N$ was found (Appendix 2). In this intermediate energy band, the hard and soft emission components may have comparable contributions. Because they are visible over distinct modulation phases, and have different modulation parameters (particularly ψ_0), the demodulation might become ineffective.

3.8 NuSTAR data in 2017 (NuS17)

We finally analyze the NuS17 data, more concisely than NuS16 because the source became ~ 4 times fainter. The demodulation analysis was conducted using the full modulation phase, by changing E_L and E_U . Since the pulsation is expected at $P = 1.01018$ s from equation (12), the search was performed, as for NuS16, in a narrow period range around the prediction. The solid black line in figure 12a is a result using $E_L = 5.1$ keV and $E_U = 12$ keV, where a minor peak appeared at a period close to the prediction.

When we limit the modulation phase to $[t/T] = 0.44 - 1.04$, the photon number was halved, but the above peak grew higher to $Z_4^2 \approx 48.6$, and became rather dominant, as shown in the same figure by a brown line with dots. Its period is determined as

$$P = 1.0101792(10) \equiv P_{17} \quad (17)$$

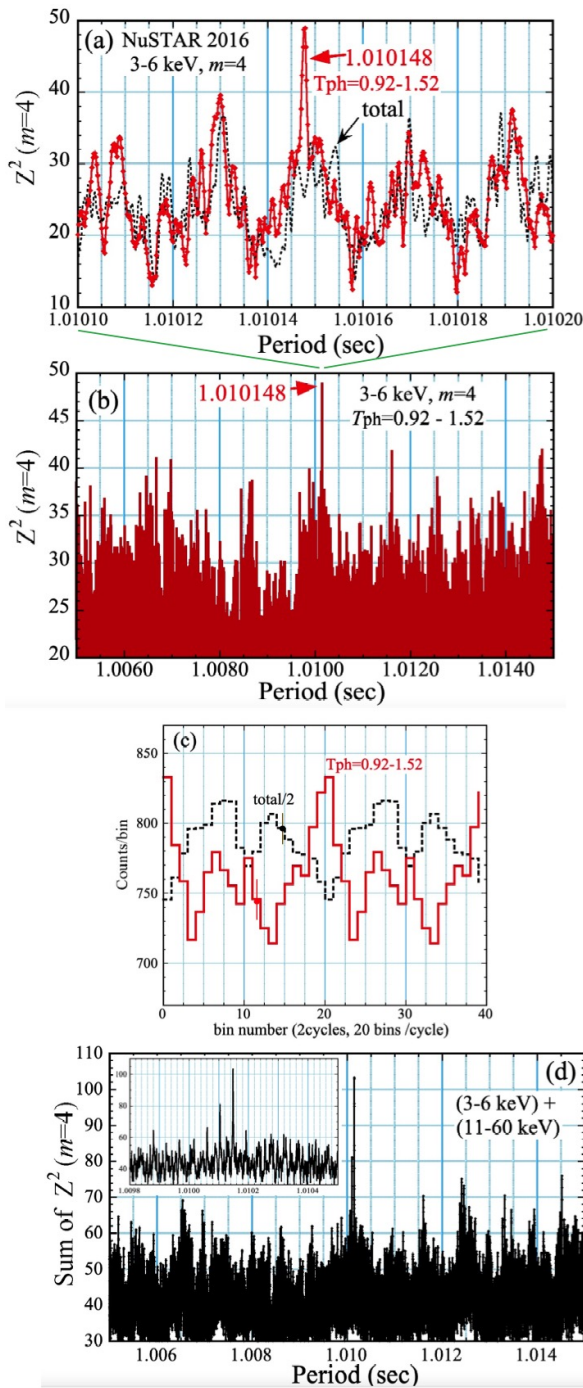


Fig. 11. Results from NuS16 in the 3–6 keV band. (a) Demodulated 3–6 keV PGs with $m = 4$, presented over a narrow period range. The PG for $[t/T] = 0.92 - 1.52$ is given by a solid red line with dots, and that for $[t/T] = 0 - 1$ by a dashed black curve. (b) The same as the red curve with dots in (a), but the period range is expanded to that of equation (7). (c) Folded pulse profiles for $[t/T] = 0.92 - 1.52$ (solid red) and $[t/T] = 0 - 1$ (dashed black; halved). (d) A sum of two PGs, one in panel (b) and the other in figure 10c. The inset expands a region around the peak. Alt Text: Same as the previous figure, but using the 3–6 kilo-electronvolt photons.

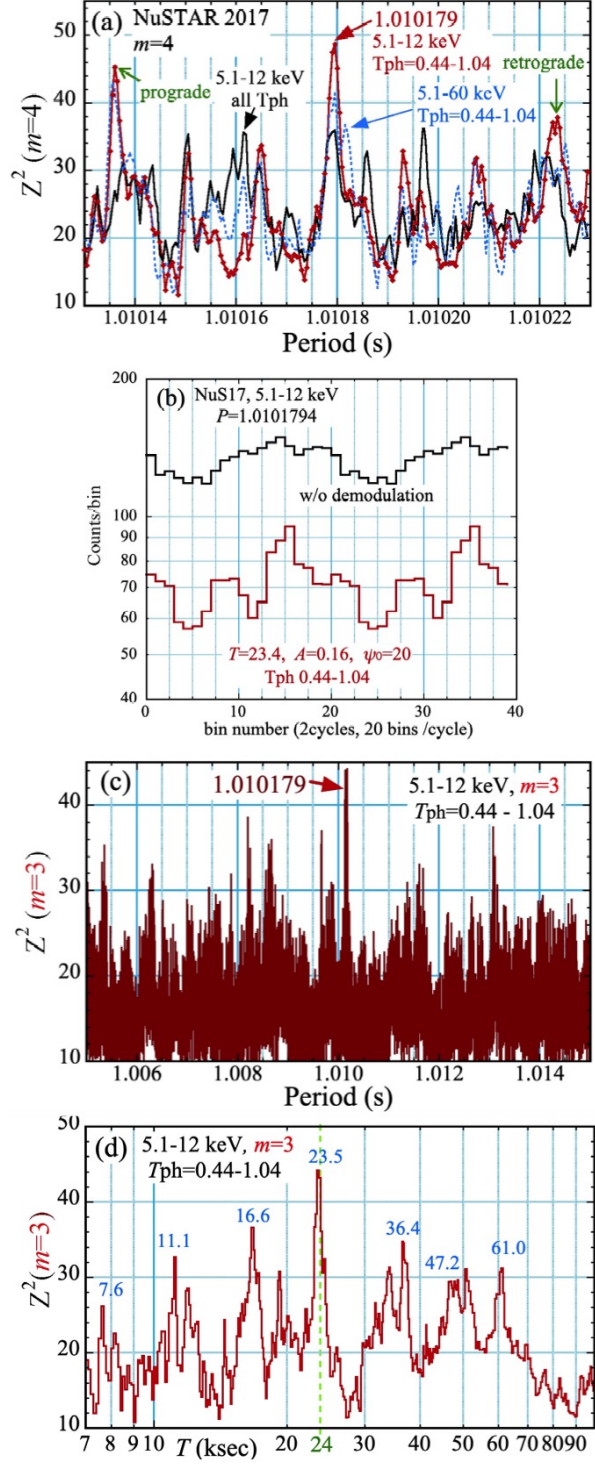


Fig. 12. Results from NuS17. (a) Three PGs with $m = 4$, shown over a narrow period range. The demodulated PG, using all photons in 5.1–12 keV, is shown in solid black. A constraint of $[t/T] = 0.44 - 1.04$ turns it into the one in solid brown line with dots. It further changes into the dashed blue one, when the energy range is expanded to 5.1–60 keV. (b) Pulse profiles in 5.1–12 keV, folded at P_{17} . The upper one is before the demodulation, using all modulation phases. The lower one is after demodulation, and limiting $[t/T]$ to 0.44 – 1.04. (c) A demodulated $m = 3$ PG in 5.1–12 keV, with $[t/T] = 0.44 - 1.04$, shown over the fiducial period range. (d) The behavior of Z_3^2 as a function of T , using the same condition as (c). Values of T are given for some peaks. Alt Text: Results from NuS17, mainly using 5.1–12 kilo-electronvolt photons.

which agrees well with the prediction.

Since the employed 5.1–12 keV interval is much narrower than the NuSTAR bandpass, we tried to expand it. When E_L is lowered to < 5.1 keV, the P_{17} peak quickly diminished, suggesting a pulse suppression below 5.1 keV. As E_U is raised from 12 keV upwards, the peak also decreased, but more gradually. As given by a dashed blue line in figure 12a, the peak is still visible for $E_U = 60$ keV. As in NuS16, the pulsation in NuS17 is likely to be present in > 12 keV, and the gradual Z_4^2 decrease could be a result of an increased background. Hereafter, we retain the 5.1–12 keV interval.

Figure 12b presents two pulse profiles in this energy range. One is before the demodulation, while the other is after applying the demodulation and limiting the modulation phase. The latter profile is much more structured than the former; again, appropriate timing corrections and optimization of the energy range are inevitable for the pulse detection. The demodulated profile exhibits 3 sub-peaks per cycle, instead of 4. This is evidenced by a rather small difference between $Z_4^2 = 48.6$ and $Z_3^2 = 44.3$ at P_{17} .

Switching to $m = 3$, we repeated the period search, but over the fiducial period interval of equation (7). As shown in figure 12c, the P_{17} peak has been confirmed to be the highest therein. This statement still remains valid when $m = 4$ is used, but the peak has a lower contrast to the surroundings. Thus, the NuS17 data are considered to have afforded another pulse detection from 1E J1613, even though the source was rather dim at that time.

Figure 12d gives the behavior of Z_3^2 , under the same condition as panel (c), but as a function of T , with P allowed to float by $\pm 2 \mu\text{s}$ around P_{17} . This yields the best estimate of T as

$$T = 23.5 \pm 0.2 \text{ ks} \quad (18)$$

which appears also deviated from 24.0 as the NuS16 result in equation (16). There, T -values of several other peaks are also given. Some may have approximate integer ratios to 23.5 ks; e.g., 7.6 ks ($\approx 1/3$), 11.1 ks ($\approx 1/2$), and 47.2 ks ($\approx \times 2$).

4 Discussion

4.1 Summary of the timing results

Based on our magnetar studies, as well as the prediction by HH02, we assumed that equation (1) is the beat period of a freely precessing NS, and its rotation period must be much shorter, but is invisible due to the PPM. By cancelling the PPM disturbance, and appropriately selecting the energy range, we tried to detect the predicted fast (~ 1 s) pulsation of 1E 1613 in the six X-ray data sets, ASCA93, XMM01, XMM05, XMM16, NuS16, and NuS17. The attempt has resulted in a success through the following steps.

Assuming the PPM period of 24.0 ks, we began the pulse search with the ASCA93 data, over the 0.3–30 s period range. The two analysis methods consistently revealed, in the 2.5–12 keV range, an outstanding periodicity at $P_{93} = 1.009356$ s, together with its strong second-harmonic signal. Employing the demodulation, we next searched the 2.5–10 keV (later 2.7–10 keV) XMM01 data for the corresponding signal, over the fiducial 1.005–1.015 s interval. The 2.7–10 keV PG revealed the highest peak at $P_{01} = 1.00963$ s, which overwhelmed other peaks by $\Delta Z_4^2 \gtrsim 8$. In the same way, the XMM05 data were analyzed over the fiducial period interval, but with the energy range expanded to 1.4–10 keV. Then, at $P_{05} = 1.009771$ s, we detected the highest peak, which exceeded other peaks by $\Delta Z_4^2 \gtrsim 5$. Because P_{93} , P_{01} , and P_{05} have modest statistical significance individually, and align well under a constant \dot{P} , they may be regarded as the pulse periods of 1E 1613.

We finally analyzed the XMM16, NuS16, and NuS17 data,

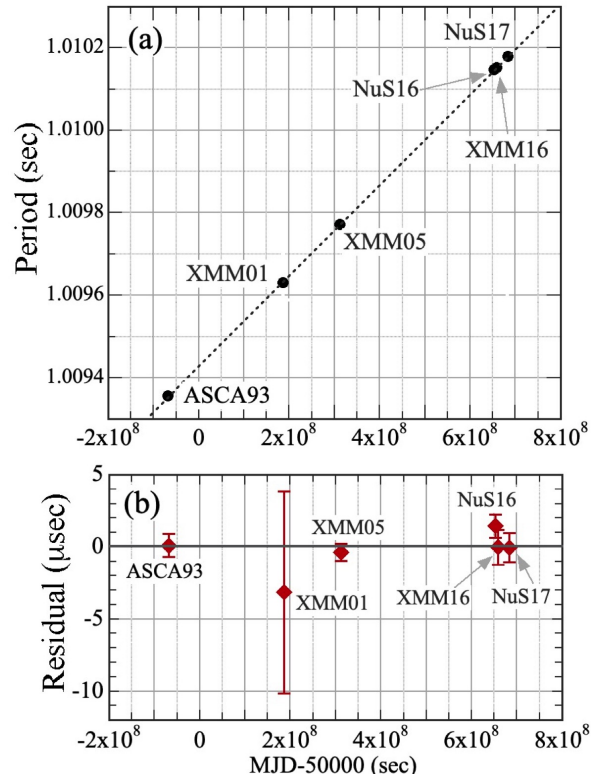


Fig. 13. (a) The six pulse periods measured from 1E 1613, shown against the time in seconds from MJD 50000.0. Measurement errors are much smaller than the plotting symbols. The fit with equation (19) is presented in a dashed line. (b) The period residuals in μs from the linear fit in (a). Alt Text: (a) The pulse periods measured in the six observations, plotted against the time. (b) Residuals from the linear fit.

all acquired after the 2016 June outburst. From XMM16, the strongest periodicity over the fiducial period interval was found at $P_{16}^X = 1.010152$ s, even though we had to discard photons below 6.6 keV. The NuS16 data afforded the pulse period of $P_{16}^N = 1.010148$ s, both in 11–60 and 3–6 keV, even though we had to use limited modulation-phase intervals which differ between the two energy bands. Through a similar demodulation analysis of the 5.1–12 keV photons from NuS17, using a limited modulation-phase interval, the pulse period was found at $P_{17} = 1.010179$ s.

Figure 13a summarizes the measured six periods as a function of time. We emphasize that these periods were all identified as the highest peak of the PG over the fiducial range (1.005–1.015 s), except for the ASCA93 result which dominates the much wider interval of 0.3–30 s. Also plotted is a linear fit, which updates equation (12) and is expressed as

$$P(t) = 1.0094300(2) + 1.097(2) \times 10^{-12} t \text{ s}, \quad (19)$$

where t is the time measured from MJD 50000.0 in sec. Thus, the data points line up precisely on the linear fit, because the fit residuals, shown in panel (b), are generally within measurement errors. No noticeable period excursions are seen, in the latest three points acquired immediately after the onset of a high activity.

4.2 Overall pulse significance

4.2.1 Statistical significance

Needless to say, the most critical issue with the present work is whether the ~ 1.01 s pulsation is real or false. As detailed in Appendix 1 and summarized in table 2, the highest- Z_4^2 period

identified in each data set has a chance occurrence probability of roughly 1 to 10 percent, except in NuS16 and NuS17 where we skipped the probability estimation (because of the difficulty in modeling the modulation-phase selection). Although these values may not be convincing enough individually, they are contingent to the selection of the period search range, and could be considerably tighter, as touched on at the end of subsubsection 3.5.1 for XMM05, and in subsection 3.6 for XMM16. Furthermore, we can utilize an obvious advantage of analyzing multiple data sets; namely, we can evaluate the overall pulse significance by combining the individual results. Below, we perform this attempt in two slightly different ways.

First, let us consider a hypothesis:

H : A real pulse period of 1E 1613 is present at ~ 1.01 s.

We regard the ASCA93 result as the prior knowledge on H , and examine how H is reinforced by the addition of the XMM01 result which is expressed by a symbol X_{01} . The posterior probability for H to still remain false, after X_{01} occurred, is given as

$$P(\bar{H}|X_{01}) = \frac{P(X_{01}|\bar{H})P(\bar{H})}{P(X_{01}|\bar{H})P(\bar{H}) + P(X_{01}|H)P(H)} \quad (20)$$

by the Bayes' formula. Here, $P(\bar{H}) = P_{ch}(P_{93}) = 0.54\% \equiv \delta$ and $P(H) \equiv 1 - \delta$ are prior probabilities for the ASC detection of pulsation to be false and true, respectively, and $P(X_{01}|\bar{H}) = P_{ch}(P_{01}) = 0.92\% \equiv \beta$ is the probability that P_{01} is detected by chance even when H is false (i.e., no intrinsic periodicity). Finally, $P(X_{01}|H) \equiv \gamma$ is a likelihood with which we expect to detect the periodicity in XMM01, when the ASCA detection is assumed true. Although γ is rather uncertain, it should not deviate significantly from unity, because ASCA93 and XMM01 have similar number of photons. Assuming $\beta\delta \ll 1$ and $\mathcal{O}(\gamma) = 1$, we find

$$P(\bar{H}|X_{01}) = \frac{\beta\delta}{\beta\delta + \gamma(1 - \delta)} \approx \beta\delta/\gamma = 5.0 \times 10^{-5}/\gamma. \quad (21)$$

Thus, even when a conservative value as, e.g., $\gamma \gtrsim 0.5$, is assumed, we obtain $P(\bar{H}|X_{01}) \lesssim 1.0 \times 10^{-4}$. By repeating the argument by further taking into account the XMM05 and XMM16 results, this value will further decrease to $\lesssim 10^{-5}$.

We may alternatively consider in the following way. Among the four P_{ch} values in table 2, those of MM01, XMM05, and XMM16 were calculated against the fiducial interval [equation (7)]. In contrast, that of ASCA93 referred to the much wider 0.3–30 s range [equation (29)]. Now that the six periods from the six data sets have all been identified as the highest peak over the fiducial period range, we are allowed to recalculate the period trial number for ASCA93, this time using the fiducial interval. This yields $N_{\text{trial}}^P \approx 1243$ instead of equation (29). Thus, considering feedback information from the other five data sets, the false probability of ASCA93 may be revised as $P_{ch}(P_{93}) \approx 1.6 \times 10^{-5}$, which is comparable to the Bayesian result.

From these two evaluations, an overall false probability may be quoted as $< 1 \times 10^{-5}$. We can now conclude that the ~ 1.01 s pulsation of 1E 1613 is real *at least statistically*.

4.2.2 Qualitative supports

Although the statistical significance of the 1.01 s periodicity has been assessed as above, this is not necessarily sufficient, because we also need to rule out systematic artifacts. This includes the case that the true pulse period resides somewhere which is slightly deviated from 1.01 s, and we are observing its side lobes. Since there is no simple way of quantifying the probability of various systematic effects, below we list qualitative pieces of evidence that are thought to strengthen the reality of the periodicity against artifacts

(both systematical and statistical).

1. In figure 13, the measured five periods very accurately line up on a constant- \dot{P} trend. This would be difficult to explain when some, if not all, of these periods were due to some artifacts (e.g., statistical fluctuations or some side lobes).
2. While the ASCA and NuSTAR data are subject to periodic data gaps synchronized with the spacecraft orbits, those of XMM-Newton to sporadic ones due to the flare removal. Their consistency hence argues against the pulsation being instrumental artifacts that are related to data gaps.
3. In ASCA93, our start point, the harmonic pulse periods were revealed consistently by the two algorithms, the phase-sorted analysis and the demodulated PGs. Therefore, the pulses are unlikely to be an algorithm-specific artifact.
4. In the ASCA93 data, the CCO photons were affected by the PPM at $T = 24.0$ ks (figure 3a), whereas the pulsar data were free from such effects over $T = 7.0 - 100$ ks (figure 3b).
5. Except in XMM05 when the source was rather faint, the demodulated pulse profiles below ~ 10 keV are very similar. They consist of a dominant main peak and a weaker sub-peak, on which the 4-peak structure is often superposed.
6. Except in XMM16, the 6.67 hr period has been identified via timing studies alone, although the NuS16 and NuS17 data favor somewhat shorter periods [equations (16) and (18)].
7. In figure 6c, the pulse periods in XMM01, determined over short intervals without demodulation, vary just as predicted by the precession scenario (subsection 4.3).
8. Both in the 11–60 keV and 3–6 keV bands, the pulses in NuS16 are clearly seen only for $\sim 50\%$ of the modulation phase (figure 10, figure 11). If P_{16}^N arose due to some artifact at least in one of these energy intervals, this sort of correlated behavior would have scarcely taken place.

4.2.3 A composite PG

As a visualization of the overall pulse significance, figure 14 shows our final composite PG, obtained as an incoherent sum of five demodulated PGs, one from each data set (except Nu17 which favors $m = 3$); figure 2b (but limiting the period range to the fiducial interval) from ASCA93, figure 5a from XMM01, figure 7a from XMM05, figure 9b from XMM16, and figure 11d from NuS16. As the only one freedom in summing up the five PGs, we converted the period in each PG to that to be recorded at the epoch of ASCA93, referring to equation (19). Consequently, the highest peaks of the five constituent PGs have all added up into an extremely prominent single peak, at a period which accurately coincide with equation (3b). The peak height, $\sum Z_4^2 = 298.4$, is lower, only by $\Delta Z_4^2 = 5.0$, than the sum of the five peak values of the constituent PGs. Details around the peak, given in the inset, reconfirm the series of side lobes that were observed in figure 2d.

4.3 Possible emission geometry

Now that we have identified the ~ 1.01 s period with the spin period of 1E 1613, we must find an emission geometry that makes the pulses directly invisible, and produce, at the same time, the large-amplitude X-ray modulation at equation (1). The former condition is not difficult, as the hard X-ray pulsation of magnetars is often undetectable, unless we conduct the demodulation with the knowledge of the soft X-ray pulse period (e.g., Makishima et al. 2021b). In contrast, the latter condition, seldom seen among mag-

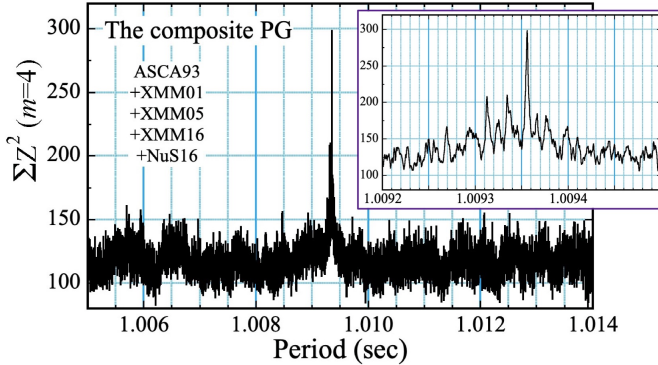


Fig. 14. The final composite PG, derived by summing up five PGs from the five data sets except NuS17 (see text). The period of each constituent PG is converted to that of ASCA93, referring to equation (19). The inset shows details around the peak, on the same scale as panels (c) and (d) of figure 2. Alt Text: The final periodogram, obtained by summing up five individual periodograms.

netars (Makishima et al. 2016, 2019), is not trivial.

Already, a successful model to explain the above two requirements has been presented by HH02, who assumed a slightly aspherical NS, and surface emission from a hot spot that is displaced from the stellar symmetry axis. The model, however, may need some modification, because the assumed simple surface emission would not explain the observed pulse profiles which are rich in fine structures. Below, we consider a revised (though very primitive) free-precession scenario, which invokes asymmetric beaming of the emission, instead of the source's positional displacement. The terminology which we have adopted in section 1 is retained.

We assume that the NS is prolately deformed by the toroidal field of $B_t \sim 10^{16}$ G, to an asphericity of $\epsilon \equiv (I_1 - I_3)/I_3 \sim 10^{-4}$ (e.g., HH02, Makishima et al. 2024a), where I_j ($j = 1, 2, 3$) are the principal moments of inertia in the coordinates $(\hat{x}_1, \hat{x}_2, \hat{x}_3)$ fixed to the star. Its symmetry axis \hat{x}_3 (to be identified with the magnetic axis) precesses around the angular momentum vector \vec{L} , with a period $P_{\text{pr}} = 2\pi I_1/|\vec{L}| = (1 + \epsilon)P_{\text{rot}}$, where $P_{\text{rot}} = 2\pi I_3/|\vec{L}|$ is the rotation period around \hat{x}_3 . The precession and rotation periods differ slightly, and their beat appears at a long period given as

$$T_{\text{sl}} = \frac{P_{\text{pr}}}{\epsilon \cos \alpha} = \frac{1}{\cos \alpha} (P_{\text{rot}}^{-1} - P_{\text{pr}}^{-1})^{-1}. \quad (22)$$

Here, α is a constant "wobbling angle" between \hat{x}_3 and \vec{L} . If the emission is symmetric around \hat{x}_3 , a strictly periodic pulsation is observed at P_{pr} (not P_{rot}), but the PPM sets in if the emission breaks the symmetry.

We identify P_{pr} with the ~ 1.01 s pulse period, and T_{sl} with T in equation (1). These yield $\epsilon \cos \alpha = P_{\text{pr}}/T_{\text{sl}} = 0.42 \times 10^{-4}$, which is typical of magnetars (Makishima et al. 2024a).

Adopting the toy model in Makishima et al. (2021a), we assume that the emission comes from one magnetic pole, in a conical beam pattern as illustrated in figure 15a. The cone is hollow, symmetric around \hat{x}_3 with a half-opening angle θ , and emits beams along its generatrices, each with a divergence angle $\pm 23.5^\circ$. To break the symmetry around \hat{x}_3 , the beam brightness is assumed to vary as $\propto 1 + a \cos \Psi$. Here, a ($0 \leq a \leq 1$) describes the degree of asymmetry, and Ψ (0 to 2π) is the cone azimuth measured in the $(\hat{x}_1, \hat{x}_2, \hat{x}_3)$ frame. (For a remote observer, Ψ appears as the modulation phase, $[t/T]$). Then, (Φ, α, Ψ) define the Euler angles from the observer frame to the stellar frame, where Φ is the pulse phase. As described in subsubsection 4.5.4, this model is analogous to that used to explain some behavior of radio pulsars.

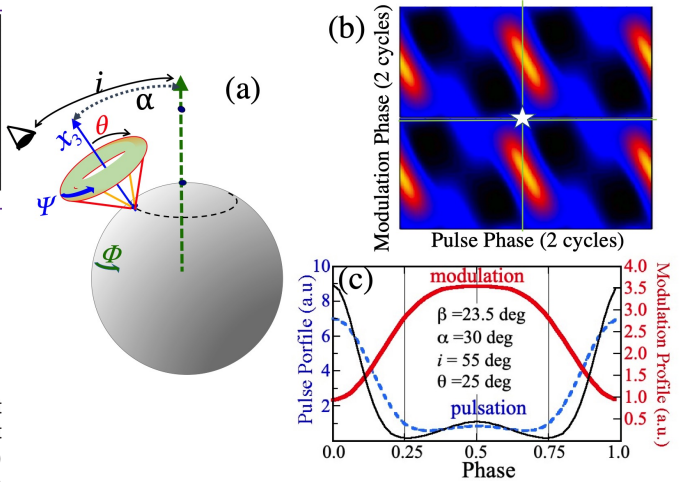


Fig. 15. (a) A possible geometry, after Makishima et al. (2021a). (b) Prediction of the model, shown as a color-coded photon intensity map on a plane of pulse phase vs. modulation-phase plane, with the photon intensity color coded. Figure 15c gives the pulse profile (dashed blue) and the modulation profile (solid red), obtained by projecting panel (b) onto the pulse-phase and modulation-phase axes, respectively. Alt Text: A possible emission geometry, together with its predictions.

Assuming $\alpha = 30^\circ$, $i = 55^\circ$ (so the emitting pole is not self-eclipsing), $\theta = 25^\circ$, and $a = 1$, we numerically calculated the expected pulse profile. The result is presented in figure 15b on a pulse-phase vs. modulation-phase plane, with the photon intensity color coded. Figure 15c gives the pulse profile (dashed blue) and the modulation profile (solid red), obtained by projecting panel (b) onto the pulse-phase and modulation-phase axes, respectively.

The result reproduces three observed properties. First, the pulse phase is modulated with an amplitude close to ± 0.25 cycles. (When fine structures are present, the pulse visibility would further decrease.) Next, the modulation profile swings from 1.0 to 3.5, by a factor 3.5 just as observed in the figure 8c inset. Finally, when the 6.67 hr flux modulation is minimum (a white star), the pulse timing delay is $\Delta t \sim 0$ and is increasing with the modulation phase, as found in subsection 3.5.

Since the adopted angles, $\alpha = 30^\circ$, $i = 55^\circ$, and $\theta = 25^\circ$, are ordinary, the results appear to apply to any magnetar. However, one secret recipe is that $i = \alpha + \theta$ holds. As a result, the brightest part of the cone directly points to us when $\Phi = \Psi = 0$, producing the bright spots in figure 15b. This may explain the peculiarity of this object. While α and i should be constant, θ and a can change with time, depending, e.g., on the luminosity. Then, the above condition can sometimes be violated, and the swing of the modulation profile will decrease. The absence of clear 6.67 hr intensity variations in the ASCA data may be thus explained.

Of course, this model is still subject to many inadequacies. It considers neither the general-relativistic light bending effects, nor emission from the other pole. No attempt has been made to reproduce the 4-peak structure seen in the pulse profiles. It is unclear if the double-peaked modulation waveform of XMM16 in figure 9a and of NuS16 in figure 10a can be explained, even though the flat-topped peak is relatively well reproduced. The pulse profile is smeared to some extent compared with the case of no PPM, but is still clearly visible without demodulation. Also, it is not obvious, either, whether the $[t/T]$ independence of the pulsation in XMM05 (figure 8c) and strong $[t/T]$ dependence in NuS16 (figure 10, figure 11) and nuS17 (figure 12) can be consistently modeled. Instead of trying to improve the model, we may quote a phrase from Makishima et al. (2021a); *figure 15 is meant to show*

that some emission geometry can roughly explain the observation, rather than to claim that the selected model or the geometrical parameters are correct.

4.4 The nature of the object

Assuming that 1E 1613 has a ~ 1.01 s spin period which changes with a rate given by equation (19), and identifying $T = 24.0$ ks with the beat period, we can derive basic properties of 1E 1613 as a young pulsar. First, the characteristic age is readily calculated as

$$\tau_c \equiv P/2\dot{P} = (14.7 \pm 0.1) \text{ kyr.} \quad (23)$$

When compared with the estimated age of RCW 103, $\tau_{\text{SNR}} = 2.0 - 4.4$ kyr (Carter et al. 2019; Braun et al. 2019), we find $\tau_c/\tau_{\text{SNR}} = 3.3 - 7.3$. This ratio is comparable to those found with other magnetar-SNR pairs by Nakano et al. (2015), who showed that the τ_c vs. τ_{SNR} discrepancy may be an artifact caused by the decay of dipole magnetic fields. Or else, invoking rather long natal pulse periods can also solve the discrepancy.

Next, the spin-down luminosity is calculated as

$$L_{\text{rot}} = (2\pi)^2 I_{45} \dot{P} P^{-3} \approx 4.2 \times 10^{34} \text{ erg s}^{-1} \quad (24)$$

where I_{45} is the moment of inertia of a NS in 10^{45} g cm 2 . Considering the typical conversion efficiency from rotational to radiative energies in pulsars, 10^{-4} to 10^{-2} (Possenti et al. 2002), and the X-ray luminosity of 1E 1613 which varies over $10^{33} - 10^{35}$ erg s $^{-1}$ (DL06), this L_{rot} can sustain, at best, the lowest observed luminosity. Therefore, 1E 1613 must be magnetically powered, at least in outbursts.

Assuming $\alpha \sim 30^\circ$ from the above model, the dipole magnetic field of this object is given as (Ostriker & Gunn 1968)

$$B_d \sim 2.2 \times 10^{19} (\sin^{-1} \alpha) \sqrt{P \dot{P}} = 4.6 \times 10^{13} \text{ G.} \quad (25)$$

This is typical of “high field pulsars” rather than magnetars, but it possibly reaches the critical field.

As to B_t , we can derive an estimate as

$$B_t \sim \sqrt{(10^4 P/T \cos \alpha)} \times 10^{16} = 7 \times 10^{15} \text{ G} \quad (26)$$

after Makishima et al. (2024a). This is only slightly lower than those of typical magnetars. Then, 1E 1613 is implied to have $B_t/B_d \sim 152$. This ratio is somewhat higher than the values of 40 to 100, which are predicted by the τ_c vs. B_t/B_d scaling found by Makishima et al. (2024a) among the seven magnetars.

The present work for the first time provided quantitative support to the view, that 1E 1613 is a magnetically-powered NS (section 1). However, we also notice several differences from typical magnetars (Olausen & Kaspi 2014), such as the shorter P (though not the shortest) and the weaker B_d . More importantly, the timing residuals of 1E 1613 (figure 13b) is much smaller than those of magnetars (e.g., $\sim 1\%$; Younes et al. 2017). In some aspects, 1E 1613 might resemble, particularly in quiescence, rotation-powered pulsars, even though its radio quietness remains to be explained.

4.5 Some additional remarks

4.5.1 Luminosity dependent effects

Through the analysis, we noticed some luminosity-dependent source properties. Namely, a luminosity decline may be accompanied by an increase in A , a decrease in the pulse fraction (table 2), a possible decrease of E_L above which equation (5) works, and changes of double-peaked profiles into 4- (or 3-) peaked ones. Interpretations of these effects, however, are not attempted here.

4.5.2 Meanings of E_U and E_L

In the present work, the pulse detection required us to optimize, in a data-dependent way, the upper (E_U) and lower (E_L) energy thresholds (table 2). Of these, the meaning of the employed E_U is rather simple to interpret, because $E_U = 12$ keV of ASCA93, $E_U = 10/12$ keV of XMM-Newton, and $E_U = 60$ keV of NuS16, are all close to the instrumental upper-limit energy. Also, as evidenced by figure 12a, $E_U = 12$ keV of NuS17 is a relatively loose boundary, above which the background gradually becomes dominant. Thus, the pulsation of 1E 1613 is likely to be always detectable in harder energies, as long as the signal statistics allow, and the PPM correction is properly performed.

The meaning of E_L , in contrast, is more difficult to understand for a few reasons. Although E_L is rather sharply specified by the individual data sets, it scatters considerably among observations (table 2). Putting aside ASCA93, E_L was at 2.7 keV (XMM01), 1.4 keV (XMM05), 6.6 keV (XMM16), 11 keV (NuS16), and 5.1 keV (NuS17). It is not yet clear what causes E_L to vary, as the suggested correlation between E_L and the luminosity is not tight enough. Last but not least, we cannot associate E_L with particular features or components in the spectra of 1E 1613 (DL06; Esposito et al. 2019; Rea et al. 2016), partly because the spectrum is rather featureless. At present, what we can suggest is the following candidates. (1) In XMM05, the spectral normalization varies with 6.67 hr, but this behavior disappears in $\lesssim 1.4$ keV (DL06). (2) In NuS16, the hard power-law component and the hotter blackbody cross over, at ~ 9 keV (Rea et al. 2016) which is close to $E_L = 11$ keV. (3) In XMM16, two blackbodies cross over at about $E_L = 6.6$ keV (Esposito et al. 2019).

In magnetars, the timing vs. spectrum relation is much clearer (Makishima et al. 2014; Makishima et al. 2024b). Their hard X-ray emission (seen in $\gtrsim 10$ keV) is thought to break the symmetry around the magnetic axis, whereas their soft X-ray emission is axially symmetric. As a result, their hard X-ray pulses are PPM affected, whereas their soft X-ray pulses are directly detectable without PPM. In contrast, the pulsation of 1E 1613 below E_L is not visible, even applying the demodulation. Therefore, as mentioned in subsection 3.6, the softer X-rays from 1E 1613 may still be affected by the PPM that cannot be adequately rectified by the simple form of equation (5). For example, in softer energies where the beam divergence must be larger, the emission from 1E 1613 may start to be contributed by the other pole, or from other regions of the same pole. If this component is beamed in a different direction, it would require a different (A, ψ_0) pair, and make the demodulation difficult.

To better understand these intriguing issues, and clarify the fundamental relation of 1E 1613 to magnetars, it may help if we examine the distribution of photons on the plane of pulse phase vs. modulation phase. Alternatively, we may produce the spectra of 1E 1613, sorted by the pulse phase and/or the modulation phase, although the photon statistics might become severe.

Considering these complex properties of 1E 1613, we were extremely lucky to have started with ASCA93. At that time, the object was luminous with a high pulse fraction, and yet the simple PPM worked down to $E_L = 2.5$ keV, which was preset with little ambiguity by the SNR contamination. If we had started from any other data sets, we may not have achieved the present results.

4.5.3 Is T time variable?

Generally, the PPM period T was consistent with equation (1), but the NuS16 data [equation (16)], and possibly the NuS17 data too [equation (18)], suggest a marginally shorter period. (The XMM16

data were inconclusive on this point.) In view of equation (22), any intrinsic change in T , if significant, should be attributed to those in P , ϵ , or α , presumably synchronized with the 2016 June activity. Of them, the change in P can be ruled out as a cause of the possible decrease in T , because \dot{P} has the opposite sign, and is way too small. An increase in ϵ could make T shorter, but we expect ϵ to gradually decrease, as the magnetic energy is spent in radiation. The most likely scenario is a sudden decrease in the wobbling angle α by $\sim 3^\circ$ across the June 2016 outburst, possibly coupled with the modulation profile change.

4.5.4 Analogy to the subpulse drifting phenomenon

The geometrical model in figure 15a has an interesting analogy to that used to describe the “subpulse drifting” phenomenon often observed from radio pulsars (e.g., Gogoberidze et al. 2005). In both cases, the system is assumed to have two rotational modes around different axes. One is around the angular-momentum vector with a period P , and produces the periodic pulsation. The other is around the magnetic axis, with a period P' , and modifies the pulsation. In the present case, $P' = P/(1 + \epsilon)$ is so close to P that the beat between P and P' appears as a PPM with the long modulation period $T = P/\epsilon \sim 10^4 P$. As to the drifting subpulse phenomenon, P' is typically 10–100 times P , and corresponds to the period P_3 in which the subpulse completes its drift across P . However, even putting aside that P_3 is much shorter than T , the two cases have a fundamental difference. Namely, P' of 1E 1613 (and magnetars) arises as rigid-body dynamics of NSs under axial deformation, whereas P' of radio pulsars is due to some magneto-plasma effects in the magnetosphere of spherical NSs.

4.6 Future tasks

The present result will become a start point of a novel paradigm for 1E 161348–5055, to be followed by a series of questions. First of all, can we reconfirm the pulsation in other archival data sets? In addition to the Chandra data, these include the 1997 ASCA data and those from XMM-Newton in 2018, which were excluded based on Criteria (v) and (iii), respectively. By thus increasing the number of pulse detections, we may better assess if the decrease in T suggested by the NuS16 and NsS17 data is real or not.

A second set of questions are related to the puzzling behavior of E_L . Namely, can we identify any spectral component that carries the PPM-affected pulsation, and explain the epoch-dependent changes of its lower threshold at E_L ? Conversely, does this object harbor a “magnetar-like” soft component that is pulsating without PPM? Or else, by improving the demodulation procedure, can we detect the pulsation below E_L from at least some data sets?

The geometrical mode, of course, must be improved, to answer such inquiries as: What is a more rigorous geometry to explain the overall properties of 1E 1613, and to what extent is that geometry special? Do the model parameters depend systematically on the source luminosity, and/or the source activity as in 2016 June? How to understand the overall $[t/T]$ dependence of the pulsation beyond the arguments in Appendix 2? How can the model explain the change in the modulation profile across the 2016 activity, from the single-peaked to double-peaked ones?

Finally, as discussed in Makishima et al. (2024a), does the present scenario apply also to some other CCOs, and/or so-called long-period radio transients (e.g., Beniamini et al. 2023), including, e.g., ASKAP J1832–0911 (Wang et al. 2025)? In the overall zoo of NSs, how can we locate 1E 1613, and clarify its relation to magnetars? These issues are all left as future tasks.

5 Conclusion

We conducted timing studies of 1E 161348–5055, the Central Compact Object of RCW 103, using six archival data sets: one from ASCA take in 1993, three from XMM-Newton (2001, 2005, and 2016), and two from NuSTAR (2016 and 2017). We obtained evidence for a ~ 1.01 s pulsation, with a combined chance probability of $< 1 \times 10^{-5}$, because the six data sets all gave ~ 1.01 s pulse periods that line up, with an accuracy of $< 10\mu$ s, on a constant spin-down trend of $\dot{P} = 1.097(2) \times 10^{-12}$ s s $^{-1}$. The pulsation, however, was not directly detectable in either data set with a simple periodogram analysis. Instead, it became detectable only after removing pulse-phase modulations occurring at the period of 6.67 hr, with which the object’s X-ray intensity is known to vary. The spin period of this NS is hence concluded to be ~ 1.01 s, which is in reality the free precession period. The 6.67 hr periodicity arises as the beat between this period, and the period of stellar rotation around the symmetry axes, which differ only by 0.4×10^{-4} in fraction. This small difference is thought to arise from the NS deformation, due to toroidal magnetic fields reaching $\sim 7 \times 10^{15}$ G (HH02). The object is implied to have a characteristic age of 14.7 kyr, a spin-down luminosity of 4.2×10^{34} erg s $^{-1}$, and dipole magnetic fields of $\sim 4.6 \times 10^{13}$ G. It is basically a magnetically powered NS, and resembles a magnetar, but in some aspects it behaves like a rotation-powered NS.

Appendix 1: Statistical significance of the periodicity

Statistical significance of a peak of height $Z_m^2 = X$, found in a PG at a period P_0 , can be estimated in the following two steps. We first quantify the statistical distribution of Z_m^2 in the data, and referring to it, derive a probability $\mathcal{P}_{\text{ch}}^{(1)}(> X)$ for a value of $Z_m^2 \geq X$ to appear by chance fluctuations in a single-trial, assuming that the data are noise dominated. Then, the final post-trial probability is obtained as $\mathcal{P}_{\text{ch}}(> X) = N_{\text{trial}} \mathcal{P}_{\text{ch}}^{(1)}(> X)$. Here, N_{trial} is the effective number of overall trials contained in the PG, which, in the present case, is factorized as $N_{\text{trial}} = N_{\text{trial}}^P N_{\text{trial}}^E$, where N_{trial}^P is the trial number in the period, and N_{trial}^E is that in selecting the optimum energy range by changing E_L and E_U . Although the maximum harmonic number m can also be varied, we do not need to consider its trial number, because we keep using $m = 4$ whenever the pulse significance is concerned. (For NsS17, we switch from $m = 4$ to $m = 3$, but do not calculate \mathcal{P}_{ch} .)

Among these trial numbers, the dominant factor N_{trial}^P may be identified with the number of independent Fourier waves contained in the PG, as

$$N_{\text{trial}}^P = \eta_{\text{hh}}(S/P_1 - S/P_2). \quad (27)$$

Here, S is again the data span, while P_1 and P_2 are the minimum and maximum periods, hence S/P_1 and S/P_2 are the maximum and minimum wave numbers, respectively. The factor η_{hh} is same as η in equation (2), but in this case represents the effect of higher harmonics; if the n -th harmonic ($n = 1, 2, \dots$) dominates, the period P would represent a wave number $\eta_{\text{hh}} S/P$ rather than S/P .

Except in limited cases (e.g., subsubsection 3.3.1) where the distribution of Z_m^2 is analytically known, the first step of this evaluation is difficult. For example, the calculation of a demodulated PG involves, at each P , many search steps in A , ψ_0 , and sometimes T , of which the trial numbers are hard to estimate. An obvious solution is to employ Monte-Carlo simulations; we produce many fake data sets that are free from any fast periodicity, and analyze them in the same way as the actual data, to construct a statistical

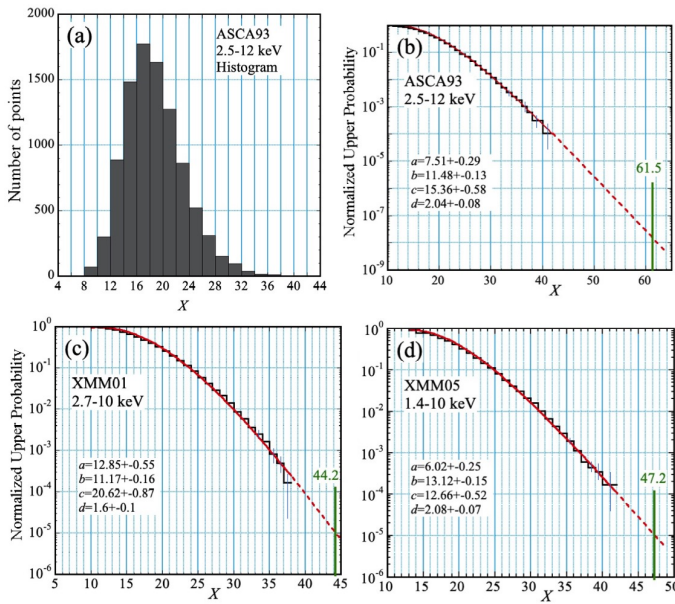


Fig. 16. (a) A histogram of 9445 samplings of Z_4^2 , obtained via a control study of the 2.5–12 keV ASCA93 data. The abscissa gives $X \equiv Z_4^2$. (b) An upper probability distribution of X , obtained by integrating the histogram in (a) from the maximum point downwards. A fit with equation (28) is shown in a red curve, and the best-fit parameter values are given in the panel. (c) The same as (b), but using the 2.7–10 keV photons from XMM01. (d) A similar result for XMM05 in 1.4–10 keV. Alt Text: Results of the control studies for ASCA93, XMM01, and XMM05.

distribution of Z_4^2 at $P \approx P_0$. However, to derive a reliable result, each fake data set must reproduce such effects as the data gaps (particularly for ASCA and NuSTAR), background variations, and the intrinsic source variation including both the 6.67 ks periodicity and sporadic changes (e.g., figure 9a).

To avoid this difficulty, the data themselves may be used instead (Makishima et al. 2023). Namely, we calculate a demodulated “control” PG, over a period range which is close to P_0 , but excludes P_0 itself as well as its major side lobes. Here, an implicit assumption is that the interval thus selected is noise dominated, and the chance probability for a noise peak with a certain height to appear at any period in the interval is the same as that at P_0 . To ensure Fourier independence between the adjacent periods, $\eta \sim 0.3$ in equation (2) is employed. Then, at each P , we maximize Z_4^2 , by scanning A and ψ_0 (as well as T in some cases), exactly in the same way as in the actual pulsation search. The derived values of maximum Z_m^2 , one from each period, are collected over a single control PG (or a few of them with different intervals), and used to produce a distribution of Z_4^2 . Previous examples are given in in Appendix B of Makishima et al. (2023).

ASCA93: We applied the above procedure to the 2.5–12 keV ASCA GIS data, to evaluate the statistical significance of Peak B in figure 2b, because our standard tool is the demodulation rather than the phase-sorted technique. Two control PGs with $m = 4$ were calculated over two period ranges, one on either side of P_{93} ; $0.80 - 1.00$ s and $1.02 - 1.22$ s, with a period step of 4.0×10^{-5} s and 4.5×10^{-5} s, respectively. These steps correspond to $\eta = 0.3 - 0.45$ in equation (2). Since the two control PGs gave consistent distributions of Z_4^2 , we co-added them, and arranged a total 9445 samplings of Z_4^2 into a histogram presented in figure 16a. The distribution is asymmetric, because small values of X are discarded when selecting the maximum Z_4^2 at each P .

By integrating the histogram, from the maximum point at $Z_4^2 = 43.3$ downwards, we obtained figure 16b, which gives the upper probability integral (Makishima et al. 2019) as a function of $X \equiv Z_4^2$. It gives the chance probability for a Z_4^2 value exceeding a given X to appear by chance, in a single trial in P . We fitted this distribution with an empirical function (Makishima et al. 2023),

$$y = \exp \left\{ a - d^{-1} \sqrt{(X - b)^2 + c^2} \right\}, \quad (28)$$

where y stands for the upper probability, while a, b, c and d are parameters. We expect $b \approx 2.0$ as an asymptotic analytic form (Makishima et al. 2023). The fitted function is superposed on figure 16b as a red curve, where the derived parameters are also given. By extrapolating the fit, Peak B with $Z_4^2 = 61.5$ was found to have $\mathcal{P}_{\text{ch}}^{(1)}(P_{93}) \approx 1.3 \times 10^{-8}$ with a typical error by a factor 1.5.

Next, equation (27) gives, in the present case,

$$N_{\text{trial}}^P = 2(S/0.3 - S/30) = 4.18 \times 10^5. \quad (29)$$

Here, we assumed $\eta_{\text{hh}} = 2$, because the folded pulse profile of ASCA93 is dominated by the 2nd harmonic (subsubsection 3.3.6). At $P \approx 1.01$ s, the implied period step is $\Delta P \approx 8.0 \mu$ s; since this is comparable to the full-width at half-maximum of Peak B ($\approx 6 \mu$ s) in figure 2d, the above estimate of N_{trial}^P is considered reasonable. When this is multiplied to $\mathcal{P}_{\text{ch}}^{(1)}$ derived above, $\mathcal{P}_{\text{ch}}(P_{93}) \approx 0.54\%$ is obtained. There is no need to consider N_{trial}^E , because we tested the 2.5–12 keV band only. We do not need to count the trial number in m , either, because the P_{93} information was derived solely from the single PG using the $m = 4$ demodulation.

XMM01: Following the procedure as for ASCA93, we calculated two control PGs, using the 2.7–10 keV XMM01 data. The selected period intervals are 0.7–1.0 s and 1.03–1.33 s, both with period steps of 1×10^{-4} . The difference from ASCA93 is due to the shorter data span, which requires more sparse period samplings, to make the adjacent ones Fourier independent. Then, a histogram of total 6000 samplings were constructed, and was converted to the upper probability distribution which is presented in figure 16c. Extrapolating a fit with equation (28), the peak at P_{01} with $Z_4^2 = 44.2$ was found to have $\mathcal{P}_{\text{ch}}^{(1)}(P_{01}) \approx 1.2 \times 10^{-5}$, with a similar uncertainty as in ASCA93.

To calculate N_{trial}^P of XMM01 from equation (27), we employed $S = 19.6$ ks and the period search range of equation (7), and set $\eta_{\text{hh}} = 2$ because the pulse profile is very similar to that in ASCA93. These yield $N_{\text{trial}}^P = 384$. Also, the choice between $E_L = 2.5$ keV and 2.7 keV gives $N_{\text{trial}}^E = 2$. The trial number in m is unity, as we tested no other values than $m = 4$. We hence obtain $\mathcal{P}_{\text{ch}}(P_{01}) = \mathcal{P}_{\text{ch}}^{(1)}(P_{01}) N_{\text{trial}}^P N_{\text{trial}}^E \approx 0.92\%$.

XMM05: The statistical significance of the 1.4–10 keV peak at P_{05} in figure 7a, with $Z_4^2 = 47.2$, was examined again in the same way as the preceding two data sets. Then, as presented in figure 16d, the peak was found to have $\mathcal{P}_{\text{ch}}^{(1)}(P_{05}) \approx 1.1 \times 10^{-5}$. On the other hand, equation (7) and $S = 87.9$ ks specify $N_{\text{trial}}^P \approx 3446$, where $\eta_{\text{hh}} = 4$ was employed in equation (27) because the XMM01 pulse profile is dominated by the 4th Fourier harmonic (subsection 3.5.2). Multiplying the above $\mathcal{P}_{\text{ch}}^{(1)}(P_{05})$ by this N_{trial}^P , and further by $N_{\text{trial}}^E \sim 5$ in the E_L scan steps (considering the energy resolution), we obtain $\mathcal{P}_{\text{ch}}(P_{05}) \approx 19\%$.

XMM16: In the same way as above, we produced a curve of upper probability, which is very similar (though not shown) to those from the preceding three data sets. An extrapolation of the fitted function by equation (28) indicates that the P_{16}^N peak in the 6.6–12 keV range has $\mathcal{P}_{\text{ch}}^{(1)} \approx 9 \times 10^{-6}$. For the period range of equation (7),

and assuming $\eta_{\text{hh}} = 3$ in view of the relatively dominant 3rd harmonic in figure 9(d1), we find $N_{\text{trial}}^{\text{P}} \approx 2382$. Further assuming $N_{\text{trial}}^{\text{E}} \approx 5$ in optimizing E_{L} , we find $\mathcal{P}_{\text{ch}} = 11\%$.

Appendix 2: Modulation-phase dependence of the pulse significance

In the NuSTAR data analysis, we found that the pulse-peak Z_4^2 can increase, in spite of a loss of photons, when we use a particular $\sim 50\%$ interval of the 24 ks cycle. We systematically studied this effect for all data sets, except XMM01 which is shorter than 24 ks, and summarize the results in figure 17. There, we calculated the Z_4^2 values of the pulsation in each data set, as a function of $[t/T]_1$ (the starting phase) which is regarded as the primary variable. Different curves specify the interval width, $\Delta[t/T] \equiv [t/T]_2 - [t/T]_1$, which serves as the secondary variable. In each panel, the dashed horizontal line in green indicates Z_4^2 derived from the entire modulation phase ($\Delta[t/T] = 1$).

NuSTAR data sets

In panel (a), the result from the 11–60 keV NuS16 data reveals a clear peak at $[t/T]_1 \approx 0.52$ and $\Delta[t/T] \approx 0.56$ (namely, $[t/T]_2 \approx 1.08$), where Z_4^2 exceeds the full-phase result by $\Delta Z_4^2 \gtrsim 15$. This increase is considered significant, because its chance probability is estimated as $\lesssim \exp(-\Delta Z_4^2/2) = 0.06\%$. The 3–6 keV NuS16 data in panel (b) exhibit very similar behavior, except that the optimum starting phase, $[t/T]_1 \approx 0.92$, is reversed from that in 11–60 keV. As in panel (c), similar behavior was also observed from the 5.1–12 keV NuS17 data. Thus, in these three cases, the pulse Z_4^2 increased significantly, when we limit the data to a particular modulation phase which has a 50% to 60% duty ratio. However, the optimum $[t/T]_1$ shows no correlation with ψ_0 in equation (5).

The 6–10 keV result from NuS16 (not shown) differed significantly. The Z_4^2 values showed a mild scatter over the range of 15 to 25 (which includes the full-phase value of 20.1), without systematic dependence on $[t/T]_1$ or $\Delta[t/T]$. Therefore, the pulsation was not confirmed even using the phase-limiting analysis. Nevertheless, these Z_4^2 values are larger than that ($\sim 2m = 8$) for purely Poissonian data. Therefore, the count rate does vary intrinsically, depending on the pulse phase and modulation phase.

The other data sets

We applied the same analysis also to the ASCA93, XMM05, and XMM16 data, and produced panels (d), (e), and (f), respectively. Although the behavior differs to some extent among them, what is common is that Z_4^2 generally stays below the dashed horizontal line. Although some data points exceed this full-phase value by $\lesssim 7$, they can be considered as statistical fluctuations, because their estimated chance probability is higher than a few percent. Therefore, the optimum solution for these data sets is to employ the entire modulation phase.

The behavior of XMM05 in (e) implies that the pulse significance remains relatively high even when we limit the modulation phase to 0.0–0.5, but this corresponds to the *minimum* phase of the 24 ks flux variation as seen in figure 8c. This apparent contradiction must be solved in our future studies.

We further examined the XMM16 and NuS17 data, by limiting the modulation phase in various ways, hoping to detect the pulsation over an energy range that is much wider than used so far. However, this attempt was unsuccessful.

A tentative interpretation

From figure 17, we may derive the following tentative interpretation. Generally, the pulse profile (amplitude, shape, and peak phase) of this object varies to a certain extent, depending on the modulation phase. On some occasions, the variation is so mild that the profiles from different phases look similar with good mutual coherence. If so, the highest Z_4^2 will be obtained by summing up the profile over the entire phase. This condition is thought to apply to panels (c), (d), and (e). On other occasions, the profile differs considerably among the phases, just as in figure 10b, and the pulse visibility would degrade by mixing up different phases. In this case, we can maximize Z_4^2 by selecting only those phases where the pulse profile remains coherent with a high visibility. Panels (a) through (c) are thought to correspond to this condition.

We are tempted to consider that the strong phase dependence was a result of the source activation in 2016 June. Although this view is suggested by the NuS16 and NuS17 results, the behavior of XMM16 argues against it. Then, the modulation-phase dependence may vary from time to time, due to some mechanisms that are unrelated to the source activity.

To further explore this intriguing phenomenon, two more attempts may be considered. As mentioned in subsubsection 4.5.2, one is to derive a series of pulse profiles from different modulation phases of the same data, and compare them quantitatively. The other is to return to the free-precessing magnetars, and search their data for the same effect. However, both these attempts will be our future tasks. In particular, the former would require accurate background subtraction and exposure correction, which we skipped in the present work.

ORCID ID

Kazuo Makishima <https://orcid.org/0000-0002-1040-8769>

Acknowledgements

The authors thank Y. Furuta, for his help in early data analysis. The present work was supported in part by the Japan Society for the Promotion of Science, grant-in-aid (KAKENHI), no.18K03694 and 24H01612. The ASCA archive is provided by the JAXA/C-SODA.

References

- Beniamini P., Wadiasingh Z., Hare J., Rajwade K. M., Younes G., & van der Horst A. J. 2023, MNRAS, 520, 1872
- Borghese, A., et al. 2018, MNRAS, 478, 741
- Braun, C., Safi-Harb, S., & Fryer, C. L. 2019, MNRAS, 489, 4444
- Brazier, K. T. 1994, MNRAS, 268, 709
- Carter, L. M., Dickel, J. R., & Boman, D. J. 1997, PASP, 109, 990
- De Luca, A. 2017, J. Phys. Conf. Series, 932, 012006
- De Luca, A., Caraveo, P. A., Mereghetti, S., Tiengo, A., Bignami, G. F. 2007, *Astrophys. Space Sci.*, 308, 231
- De Luca, A., Caraveo, P. A., Mereghetti, S., Tiengo, A., & Bignami, G. F. 2006, *Science*, 313, 814 (DL06)
- Esposito, P., et al. 2019, A&A, 626, A19
- Garmire, G. P., Pavlov, G. G., Garmire, A. B., & Zavlin, V. E. 2000, IAU Circular 7350
- Gogoeridze, G., Machabeli, G. Z., Melrose, D. B., & Luo, Q. 2005, MNRAS360, 669
- Gotthelf, E. V., Petre, R., & Hwang, U. 1997, ApJL, 487, L175 (GPH97)
- Gotthelf, E. V., Petre, R., & Vasish, G. 1999, ApJL, 514, L107
- Heyl, J. S., & Hernquist, L. 2002, ApJ, 567, 510 (HH02)
- Landau, L. D., & Lifshitz, E. M. 1996, Mechanics (3rd.ed), Pergamon

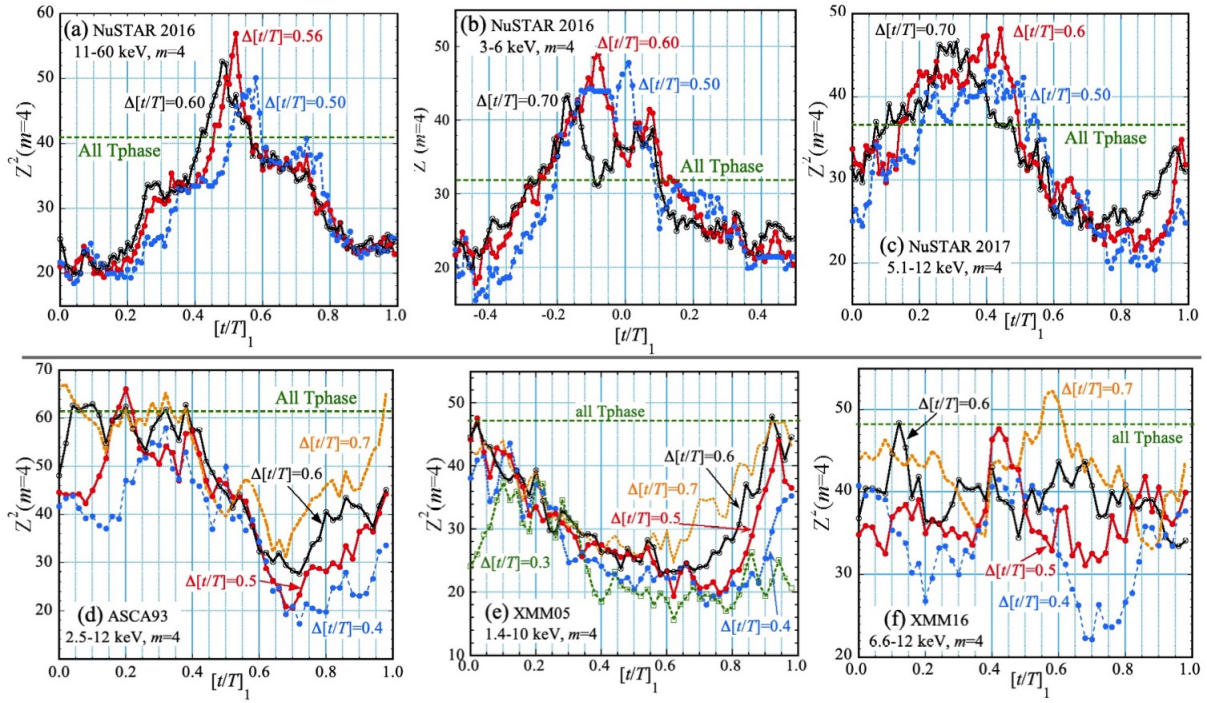


Fig. 17. The Z_4^2 value of the pulsation in each data set, shown as a function of the starting phase $[t/T]_1$ of the 24 ks modulation (see text). The effect of changing the modulation-phase width, $\Delta[t/T]$, is represented by different curves (with different symbols/colors). The dashed horizontal line indicates the Z_4^2 value obtained without limiting the modulation phase. The employed data set and energy range are given in the title of each panel. Alt Text: Effects of limiting the modulation phase on the pulse significance.

Makishima, K., et al. 1996, PASJ, 48, 171
 Makishima, K., Enoto, T., Hiraga, J. S., Nakano, T., Nakazawa, K., Sakurai, S., Sasano, M., & Murakami, H. 2014, Phys. Rev. Lett., 112, 171102
 Makishima, K., Enoto, T., Murakami, H., Furuta, Y., Nakano, T., Sasano, M., & Nakazawa, K. 2016, PASJ, 68, S12
 Makishima, K., Enoto, T., Yoneda H., & Odaka, H. 2021a, MNRAS, 502, 2266
 Makishima, K., Murakami, H., Enoto, T., & Nakazawa, K. 2019, ApJ, 71, 15
 Makishima, K., Tamba, T., Aizawa, Y., Odaka, H., Yoneda, H., Enoto, T., & Suzuki, H. 2021b, ApJ, 923, 63
 Makishima, K., Uchida, N., & Enoto, T. 2024a, MNRAS, 532, 4535
 Makishima, K., Uchida, N., & Enoto, T. 2024b, PASJ, 76, 688
 Makishima, K., Uchida, N., Yoneda, H., Enoto, T., & Takahashi, T. 2023, ApJ, 959, 79
 Nakano, T., Murakami, H., Makishima, K., Hiraga, J. S., Uchiyama, H., Kaneda, H., & Enoto, T. 2015, PASJ, 67, 9
 Ohashi, T., et al. 1996, PASJ, 48, 157
 Olausen, S. A., & Kaspi, V. M. 2014, ApJS, 212, 6
 Ostriker, J. P., & Gunn, J. E. 1969, ApJ, 157, 1395
 Pizzolato, F., Colpi, M., De Luca, A., Mereghetti, S., & Tiengo, A. 2008, ApJ, 681, 530
 Possenti, A., Cerutti, R., Colpi, M., & Mereghetti, S. 2002, A&A387, 993
 Rea, N., Borghese, A., Esposito, P., Coti Zelati, F., Bachetti, M., Israel, G. L., & De Luca, A. 2016, ApJL, 828, L13
 Torii, K., et al. 1998, ApJ, 494, L207
 Torii, K., Gotthelf, E. V., Vasisht, G., Dotani, T., & Kinugasa, K. 2000, ApJ, 534, L71
 Tuohy, I., & Garmire, G. 1980, ApJL, 239, L107
 Wang, Z., et al. 2025, Nature, 642, 583
 Younes, G., Baring, M. G., Kouveliotou, C., Harding, A., Donovan, S., Göğüş, E., Kaspi, V., & Granot, J. 2017, ApJ, 851, 17
 Zhu, W. W., & Xu, R. X. 2006, MNRAS365, L16